International Journal of Multiphase Flow 191 (2025) 105334

Contents lists available at ScienceDirect

International Journal of Multiphase Flow

journal homepage: www.elsevier.com/locate/ijmulflow

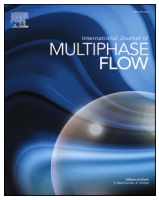

Research Paper

An improved, Rayleigh-Plesset based homogeneous cavitation model accounting for microbubble behaviour and turbulent interaction

Álvaro Pardo Vigil, Laura Suárez Fernández, José González Pérez, Adrián Pandal *

Universidad de Oviedo, Área de Mecánica de Fluidos, Campus de Viesques s/n, 33204 Gijón, Asturias, Spain

ARTICLE INFO

Keywords:
cavitation
Bubble dynamics
Turbulent interaction
Phase change
Homogeneous mixture

ABSTRACT

A new cavitation model for CFD (Computer Fluid Dynamic) calculations is developed in the present article. The model is designed to reproduce the dynamics of both microbubbles and macroscopic cavities. It is built in the frame of the homogeneous mixture URANS (Unsteady Reynolds-Averaged Navier-Stokes) equations and introduces Rayleigh-Plesset bubble dynamics. The model also accounts for surface tension, viscosity, slip velocity and the presence of noncondensable gases in the fluid. The influence of turbulence is considered based on the pressure drop arising from interactions between microbubbles and turbulent eddies. Such approach implies that, when bubble size rises, the adjacent flow turbulence is also increased resulting on additional cavitation. The new model is firstly calibrated and validated comparing its results for the well-known injector nozzle experiments from Sou et al. (2007). Different cavitating regimes ranging from inception to developed cavitation, including hydraulic flip, are analysed. In all cases, the proposed formulation allows to capture single bubble behaviour as accurately as Lagrangian modeling while maintaining the cost-effectiveness and the suitability for macro-cavitation of the Eulerian models. Comparison with the full differential Rayleigh-Plesset equation shows that the presented model is able to describe single bubble behaviour. This represents a significant improvement during the inception stage, in which isolated bubble dynamics are responsible for cavitation.

1. Introduction

The prediction of cavitation inception and development in fluid machinery has traditionally been a topic of major concern in the field of hydrodynamics. The deleterious effects of cavitation-driven bubble implosion near surfaces (Fortes-Patella et al., 2013), which violently damage the material while increasing noise and vibration, represent an engineering challenge. The design of a wide variety of industrial equipment, ranging from ship propellers (Viitanen et al., 2022) to pumps (Mousmoulis et al., 2019) and turbines (Wu et al., 2022), requires the avoidance or, at least, the control of cavitation. For this reason, extensive experimental testing is carried out as a result of the difficulty to analytically forecast the occurrence of this phenomenon (Susan-Resiga et al., 2004). There exist, however, applications for which the advantageous properties of cavitation are sought such as ultrasound cleaning (Yamashita and Ando, 2019), surface finishing processes (Manickam and Ashokkumar, 2014) or fuel injection systems (Sou et al., 2014).

Despite the abundant branches of fluids engineering benefitting from research on this field, no consensus has been attained on the most accurate method to simulate cavitating flows. Consequently, although the use of a reliable numerical model would imply a substantial reduction of product development time and cost, experimental testing is still unavoidable. What is more, experimental results and numerical predictions often differ substantially. The causes for this discrepancy do not lie on the lack of efforts towards computational modelling of cavitation but on the elusive nature of the phase change process. Heterogeneous factors including fluid composition, temperature, turbulence or surface finish (Brennen, 2013) strongly condition flow features. These are, however, difficult to incorporate in CFD calculations due to a problem of scale: the mesh quality needed to solve the macroscopic flow features and the turbulence modelling equations is rarely fine enough to deal with the microscopic bubble dynamics thar govern cavitation.

Unsteady cavitating flows are governed by a rich variety of characteristic phenomena, such as re-entrant jets and detached bubble cloud dynamics. Although cavitation commonly begins in the form of microbubble growth after the activation of nuclei in a low-pressure zone (Brandner et al., 2022), subsequent coalescence ends up forming a homogeneous macrocavity. This alters flow patterns, the cavity therefore

* Corresponding author.
E-mail addresses: pardoalvaro@uniovi.es (Á. Pardo Vigil), UO282395@uniovi.es (L. Suárez Fernández), aviados@uniovi.es (J. González Pérez), pandaladrian@uniovi.es (A. Pandal).

https://doi.org/10.1016/j.ijmultiphaseflow.2025.105334
Received 10 January 2025; Received in revised form 15 May 2025; Accepted 16 June 2025
Available online 17 June 2025

Nomenclature

Roman letters

A_B	Interfacial area volumetric density
C_D	Drag coefficient
C_μ	Turbulent viscosity constant in the $k-\varepsilon$ model
C_ρ	Compressibility correction of turbulent viscosity
$\partial x/\partial y$	Partial derivative of x with respect to y (Eulerian)
Dx/Dy	Partial derivative of x with respect to y (Lagrangian)
E_{DDES}	Dissipation term in DDES model
f	Shedding frequency
f_b	Blending function between URANS and LES
F_{DDES}	Boundary layer shielding factor in DDES
$\vec{g}$	Earth gravity acceleration
h	Mean cell size
I	Identity matrix
k	Turbulent kinetic energy
K_G	Ideal gas constant of air
l_0	Integral turbulent length scale
n	Total nuclei volumetric concentration
$N(R)$	Population number density of nuclei with radius R
p	Static pressure
p^T	Total pressure
Δp	Pressure difference across a bubble, $\Delta p = p_B - p_\infty$
$\overline{p}$	Mean static pressure in turbulent flow
p_1	Upstream pressure (at the injector inlet)
p_∞	Liquid pressure outside the bubble
p_B	Pressure inside the bubble
p_{outlet}	Outlet pressure at the nozzle end
p_{ref}	Reference pressure
p_V	Vapour pressure at saturation conditions
p_V^{turb}	Turbulence-corrected vapour pressure
p_V^{corr}	Turbulence correction for the vapour pressure
R	Bubble radius
R_0	Initial bubble radius
R_{30}	Volumetric average bubble radius
Re	Reynolds number, $Re = \frac{V_N\ W_N}{\nu_L}$
S_{cav}	Cavitation source term
t	Time
Δt	Time step
T	Cavity shedding period, temperature
$\vec{V}$	Flow velocity
$\vec{V_L}$	Liquid phase velocity
$\vec{V_B}$	Bubbly phase velocity
$\vec{V}_{B,L}$	Relative bubble slip velocity with respect to the liquid phase
V_N	In-nozzle velocity
w	Buoyancy parameter of bubbles in turbulent eddies
W_N	Nozzle width
y^+	Non-dimensional wall distance Y plus

Greek letters

α	Void fraction
ξ	Estimated minimum nuclei size
$\mathscr{S}$	Surface tension in the vapour-liquid interface
Δ	Grid spacing
ε	Turbulent kinetic energy dissipation rate, relative error
ε	Shape factor of nuclei number density distribution
γ	Polytropic expansion/compression coefficient
γ_γ	Time ratio between the turbulent eddy timescale and the particle relaxation time
Γ_t	Turbulent diffusivity
λ	Taylor turbulence scale
μ_B	Bubbly phase viscosity
μ_L	Liquid phase viscosity
μ_t	Turbulent viscosity
μ_T	Total mixture viscosity
ν_L	Liquid phase kinematic viscosity
ρ_B	Bubbly phase density
ρ_G	Noncondensable gas density
ρ_L	Liquid phase density
ρ_T	Total mixture density
ρ_V	Vapour phase density
P	Nondimensional turbulent pressure fluctuation $\mathrm{P} = \frac{3}{2}\frac{p_{fluct}}{k\ \rho_L}$
$\overline{\mathrm{P}}$	Arithmetic mean nondimensional turbulent pressure fluctuation
$\Delta\overline{\mathrm{P}'}$	Nondimensional *shifting* correction of vapour pressure
P'_{RMS}	Nondimensional *widening* correction of vapour pressure, RMS amplitude of the nondimensional turbulent pressure fluctuations
σ	Cavitation number, $\sigma = \frac{p_{outlet}-p_V}{\frac{1}{2}\rho_L V_N^2}$
σ_t	Prandtl/Schmidt number, $\sigma_t = 0.75$
ϑ	Volume

Acronyms

CFD	Computational Fluid Dynamics
DDES	Delayed Detached Eddy Simulation
DES	Detached Eddy Simulation
GCI	Grid Convergence Index
LES	Large Eddy Simulation
PISO	Pressure-Implicit with Splitting of Operators
URANS	Unsteady Reynolds-Averaged Navier-Stokes

becoming unstable as the conditions that promoted its formation are no longer present (Callenaere et al., 2001). A high-speed jet of liquid is then directed towards the low-pressure zone where the cavity is located, helped by flow recirculation downstream the cavity endpoint. The incident re-entrant jet breaks up the cavity, thus forming a detached bubble cloud that undergoes subsequent condensation (Venning et al., 2022). This breakup-detachment-condensation cycle gives rise to complex unsteady dynamics, with different regimes defined by Brennen (1994) as bubble cavitation, blade (or attached) cavitation and backflow cavitation.

The dynamics of single bubbles subjected to a known pressure field have been widely studied, with the Rayleigh-Plesset (Plesset, 1949) and the Keller-Miksis (Keller and Miksis, 1980) equations standing as the reference in incompressible and compressible fluids, respectively. Good agreement of analytically predicted bubble behaviour with the experimental data has been reached in multiple scenarios (Koukouvinis et al., 2016), as long as coalescence, nucleation and breakup phenomena are laid aside. In most practical situations, however, the behaviour of cavities (which form as a result of bubble coalescence and nucleation) differs from that of isolated bubbles. This duality has led to the emergence of finite volume methods coupling the governing equations of the (at least two) phases involved, which have adopted one of the following strategies: Eulerian reference system for the liquid phase together with Lagrangian particle tracking for bubbles (Lyu, 2020), Eulerian approach for both liquid and vapour phases involving interface capturing, or the homogeneous mixture approach. The latter is the computationally least demanding alternative, and therefore the most employed by researchers and commercial software.

In order to balance the advantages of Lagrangian (adequate for single bubbles) and Eulerian (more appropriate for cavities) reference frames, multiscale approaches have been developed. What is more, significant efforts have been directed towards their improvement since the pioneering work of Vallier (2013), with nucleation (Hsiao et al., 2017) or compressibility (Zhao et al., 2024) effects being included in models with growing sophistication. In these computational codes, a transition based on mesh resolution takes place allowing to model macrocavities by means of a mixture approach while sub-grid-sized bubbles are handled by a Lagrangian solver (Wang et al., 2023). Considerable improvements can be attained by applying such paradigm in cavitating turbulent flows (Wang et al., 2021), although the mathematical complexity and computational cost remain high when compared to strictly Eulerian alternatives.

As a consequence of the above, homogeneous mixture modelling still represents the current industrial standard, and different cavitation models have been developed in this spirit (Singhal et al., 2002; Zwart et al., 2004). The Schnerr-Sauer formulation is the alternative preferred by most researchers (Savio et al., 2021) due to its compromise between accuracy and numerical stability. Yet, limitations regarding the modelling of nucleation, cavity deformation and phase interaction are inherent to the homogeneous approach. Population balance models (De Giorgi et al., 2019) have recently been implemented in order to improve the performance of such computations, but the mathematical complexity and computational effort are significantly increased. Other recent improvements of these models include the introduction of thermodynamic effects (Li et al., 2018), slip velocity or non-dissolved gas content (Arabnejad et al., 2023). Nevertheless, the presence of microbubbles in equilibrium above the vapour pressure is neglected by all of the above, thus partially obviating the critical role played by the fluid's initial bubble content in the final results (Brandner et al., 2022). Application of these models has shown that pre-existing nuclei introduced as an inlet boundary condition collapse as soon as pressure rises above the saturation level. As a result, the onset of cavitation is underestimated and an additional pressure drop is thus required for inception, which is consequently delayed with respect to the experimental observations.

The present study introduces a novel derivation of the homogeneous mixture model in which the behaviour of microbubbles is captured by applying an extended formulation of the Rayleigh-Plesset equation neglecting second-order terms. Additionally, the vapour and non-dissolved gas are combined in a single, compressible phase to account for initial nuclei size variability, which is absent from most cavitation models. Compressibility, turbulence and slip velocity corrections based on previous works in the field are also incorporated with the aim of developing an efficient algorithm to be applied at industrial-aimed URANS simulations under the usual mesh requirements for these cases.

The development and validation of the aforementioned model is presented in the present article. In first place, a detailed mathematical derivation of the proposed model is provided starting from the description of the homogeneous mixture model and its governing equations. The translation of Rayleigh-Plesset single bubble dynamics from the Lagrangian to the Eulerian framework is detailed together with a description of the compressibility, turbulence and non-dissolved gas corrections. Consecutively, model validation is carried out following a methodology based on the Sou et al. (2007) injector experiments. A discussion on the influence of the compressibility and slip velocity terms is included, as well as a sensitivity study regarding initial bubble size and non-condensable gas content. A comparison of the model performance with respect to the full Rayleigh-Plesset equation is also provided, after which the pertinent conclusions and concluding remarks are enunciated together with suggested future works on the topic.

2. Mathematical derivation

A system of five differential convection-diffusion equations, namely continuity, momentum, vapour transport, turbulent kinetic energy transport and turbulence dissipation rate transport, is solved using a finite volume method implementing a homogeneous mixture multiphase model. Heat exchange processes are neglected, and the non-condensable gas compressibility and slip terms in the vapour transport equation can be simplified for reduced computational cost without significantly compromising accuracy. A description of the homogeneous mixture model is provided in first place, followed by a discussion on the modelling of single bubble dynamics and natural bubble populations in fluids. The cavitation source term of the present model is subsequently derived based on the translation from the Lagrangian to the Eulerian frame. Finally, the effects of slip velocity and turbulent interactions are discussed and introduced in the governing equations of the model.

2.1. Governing equations and mixture model

The Unsteady Reynolds-Averaged Navier-Stokes equations for incompressible, isothermal flow are solved for the total flow field. Phase-averaged density ρ_T and viscosity μ_T are computed as a function of the properties of each phase by means of the void fraction α:

$$\begin{cases} \rho_T = (1-\alpha)\rho_L + \alpha\rho_B \\ \mu_T = (1-\alpha)\mu_L + \alpha\mu_B \end{cases} \tag{1}$$

Under the homogeneous mixture approach, equivalent to the assumption of a dispersed interface in which the vapour phase is completely dissolved in the form of microscopic bubbles in the liquid medium, it is possible to express continuity:

$$\frac{\partial \rho_T}{\partial t} + \nabla\cdot\left(\rho_T \vec{V}^{\rightarrow}\right) = 0 \tag{2}$$

and momentum conservation:

$$\frac{\partial\left(\rho_T \vec{V}^{\rightarrow}\right)}{\partial t} + \nabla\cdot\left(\rho_T \vec{V}^{\rightarrow}\cdot\vec{V}^{\rightarrow}\right) = -\nabla p + \nabla\cdot(\mu_T+\mu_t)\left[\nabla\vec{V}^{\rightarrow} + \left(\nabla\vec{V}^{\rightarrow}\right)^T - \frac{2}{3}\nabla\cdot\vec{V}^{\rightarrow} I\right] + \rho_T \vec{g}^{\rightarrow} \tag{3}$$

for the whole mixture as if it were a single phase. The two equations of the standard $k-\varepsilon$ model are solved for turbulence closure. This model is extensively applied to cavitation simulations and is suitable for a general-purpose model due to its reliability in both cavitating and noncavitating flows. The turbulent viscosity μ_t is therefore computed as:

$$\mu_t = C_\rho C_\mu \frac{k^2}{\varepsilon} \tag{4}$$

with $C_\mu = 0.085$. When cavity shedding dynamics come into play, however, the $k-\varepsilon$ model is not able to adequately reproduce the re-entrant jet phenomenon (Callenaere et al., 2001) and the cavity shedding frequency. Specific corrections based on local flow compressibility modelled by the Tait equation have been developed and successfully validated against experimental results (Chebli et al., 2021), and hence the C_ρ expression proposed by Coutier-Delgosha et al. (2003) is incorporated to the present model:

$$C_\rho = \rho_B + \left(\frac{\rho_B - \rho_T}{\rho_B - \rho_L}\right)^{10}(\rho_L - \rho_B) \tag{5}$$

A clipping factor of 10 is used to limit the turbulent kinetic energy production (Menter and Sechner, 2021), and an enhanced wall treatment is applied to ensure accuracy in the boundary layer region.

An additional vapour transport equation is solved in the mixture model to account for bubble growth, collapse, and convective transport:

$$\frac{\partial}{\partial t}(\alpha\,\rho_B) + \nabla\cdot\left(\alpha\,\rho_B\,\vec{V}_B^{\rightarrow}\right) = S_{cav} \tag{6}$$

The cavitation source term S_{cav} is the most critical term in this expression and the main differences between cavitation models arise in its derivation, which will be henceforth described for the new approach being presented.

2.2. Single bubble dynamics

The Rayleigh-Plesset equation, resulting from the integration of the Navier-Stokes equations in a control volume delimited by the bubble-liquid interface (Brennen, 2013), describes the radial growth of a bubble subjected to an outside far-field pressure p_∞ considering the effects of viscosity and surface tension:

$$\frac{p_B - p_\infty(t)}{\rho_L} = \frac{3}{2}\left(\frac{DR}{Dt}\right)^2 + R\frac{D^2 R}{D t^2} + \frac{4}{\rho_L}\frac{\mu_L}{R}\frac{DR}{Dt} + \frac{2}{\rho_L}\frac{\mathscr{S}}{R} \tag{7}$$

Although the use of the full Rayleigh-Plesset equation for CFD computation of cavitating flows is feasible (Muzaferija et al., 2017), the second order term will be neglected in this work in order to favour numerical stability and enhance convergence speed as this equation is known to be numerically stiff (Gadi Man and Trujillo, 2016). By rearranging the terms, a second order polynomial is attained:

$$\left[\frac{3}{2}\right]\left(\frac{DR}{Dt}\right)^2 + \left[\frac{4}{\rho_L}\frac{\mu_L}{R}\right]\frac{DR}{Dt} + \left[\frac{2}{\rho_L}\frac{\mathscr{S}}{R} - \frac{p_B - p_\infty(t)}{\rho_L}\right] = 0 \tag{8}$$

This can readily be solved, yielding an analytical expression for the radial growth rate:

$$\frac{DR}{Dt} = -\left(\frac{4\mu_L}{3\rho_L}\right)\frac{1}{R} \pm \sqrt{\left(\frac{16\mu_L^2}{9\,\rho_L^2}\right)\frac{1}{R^2} - \left(\frac{4\mathscr{S}}{3\rho_L}\right)\frac{1}{R} + \frac{2}{3\rho_L}(p_B - p_\infty(t))} \tag{9}$$

This formulation of the bubble growth rate, which will be used along the subsequent deduction procedure of the source term, allows to consider viscous and surface tension effects which vary depending on the substance under study. Other cavitation models, such as Schnerr-Sauer (Sauer, 2000), employ a simpler form of (9) given by Rayleigh's equation (Rayleigh, 1917), thus neglecting bubble equilibrium effects introduced by the surface tension and the growth dynamics promoted by the effect of liquid viscosity:

$$\frac{DR}{Dt} = \pm\sqrt{\frac{2}{3\rho_L}(p_B - p_\infty(t))} \tag{10}$$

Equation (10), although simple and numerically stable, involves several simplifications concerning bubble dynamics that are overcome by the proposed expression (9).

2.3. Bubble populations and non-dissolved gas content

Although single bubble dynamics play a key role in the inception and development of cavitation, the phase change rate is also strongly conditioned by the total amount of bubbles present in the liquid. For this reason, a link between single bubble radius and total void fraction must be provided in order to translate the Lagrangian bubble behaviour to the total Eulerian reference frame used in finite volume calculations. For pure vapour bubbles, equilibrium above the saturation pressure is not possible and therefore it would be expected that no pre-existing bubbles should be found in a liquid at normal conditions (NTP). However, the presence of heterogeneous nucleation sites (namely nuclei) in the form of particles or microorganisms, in addition to a variable concentration of non-dissolved gases, allow the existence of natural bubble populations at rest.

Extensive bibliography has focused on the measurement and analysis of bubble populations, employing two main technologies: on the one hand, dynamic light scattering allows to easily register the number and size of microscopic bodies crossing a concentrated light source (Langley, 1984) but fails at discriminating bubbles from the rest of nuclei present in the fluid. On the other hand, holography requires careful post-processing but allows to monitor pure bubble populations (O'Hern, 1987). As a result, probability distributions of nuclei differ depending on the measurement technique, light scattered samples exhibiting greater population densities. However, global trends in bubble size distribution are analogous in both cases regardless of water temperature, salinity, turbulence or gas content, allowing to fit the probability density function $N(R)$:

$$N\left(R = \frac{R_2 + R_1}{2}\right) = \frac{\sum\left[\frac{Nuclei\ counts}{m^3} : R \in (R_1, R_2)\right]}{R_2 - R_1} \tag{11}$$

to a general expression proposed by Liu and Brennen (1998):

$$N(R) = n\frac{\log_{10}(e)}{\sqrt{2\,\pi}\,\epsilon\,R}\,\exp\left(-\frac{\left(\log_{10}(R) - \log_{10}(\xi)\right)^2}{2\,\epsilon^2}\right) \tag{12}$$

Where n denotes the total nuclei concentration per unit volume of liquid-vapour mixture in the sample and ξ the size of the smallest nuclei. This function is commonly plotted in log-log axes as represented in Fig. 1, taking the form of a second order polynomial to which data can be fitted using linear least squares to find n, ξ and ϵ:

$$\ln(N) = \left[-\frac{1}{2\epsilon^2}\right]\log_{10}^2(R) + \left[\frac{\log_{10}(\xi)}{\epsilon^2} - \ln(10)\right]\log_{10}(R) + \left[\ln\left(n\frac{\log_{10}(e)}{\epsilon\sqrt{2\pi}}\right) - \frac{\log_{10}^2(\xi)}{2\epsilon^2}\right] \tag{13}$$

Typical bubble populations in water measured using holography are plotted with dashed lines in Fig. 1 while those obtained by light scattering are drawn in continuous trace, representing the probability density function $N(R)$ against bubble radius R in a log-log axis. The extraordinary variability of such distributions can be verified, and shows the strong influence of the working fluid on the boundary conditions for any cavitation problem. In absence of a specific measurement of these populations, one of the options from the bibliography should be assimilated to the fluid of interest attending to criteria such as temperature, air content or even microphotography. Even though it is commonly considered that bubble population density distributions follow a power law (Alamé and Mahesh, 2024), the magnitude of its slope decreases at lower bubble radii (Yunqiao et al., 2023). This can be seen, for instance, in the distributions obtained by Arndt and Keller (1976) as provided in Fig. 1. To account for this variation, Eq. (12) has the advantage of representing a parabola in logarithmic coordinates, allowing to faithfully represent the true shape of the curve. For modelling purposes, however, the volumetric average radius will be used, thus reducing the influence of the curve shape.

It shall be remarked that, for all the empirical data plotted in Fig. 1, bubble radii above 20 μm are not at all uncommon, and the explanation for this equilibrium state lies on the initial air content. A bubble in equilibrium must fulfil the well-known condition:

$$R = \frac{2\,\mathscr{S}}{\Delta p} = \frac{2\,\mathscr{S}}{p_B - p_\infty} \tag{14}$$

Hence, positive equilibrium radii are not possible above the vapour pressure $p_B = p_V$ in the case of pure vapour nuclei. Multiphase nuclei, however, include a fraction of the non-dissolved air released by the liquid and can exist as long as the partial pressure of such non-condensable gas is:

$$p_G = p_\infty - p_V + \frac{2\mathscr{S}}{R} \tag{15}$$

The total void fraction in the fluid is equal to the ratio between the bubble volume and the total mixture volume, namely:

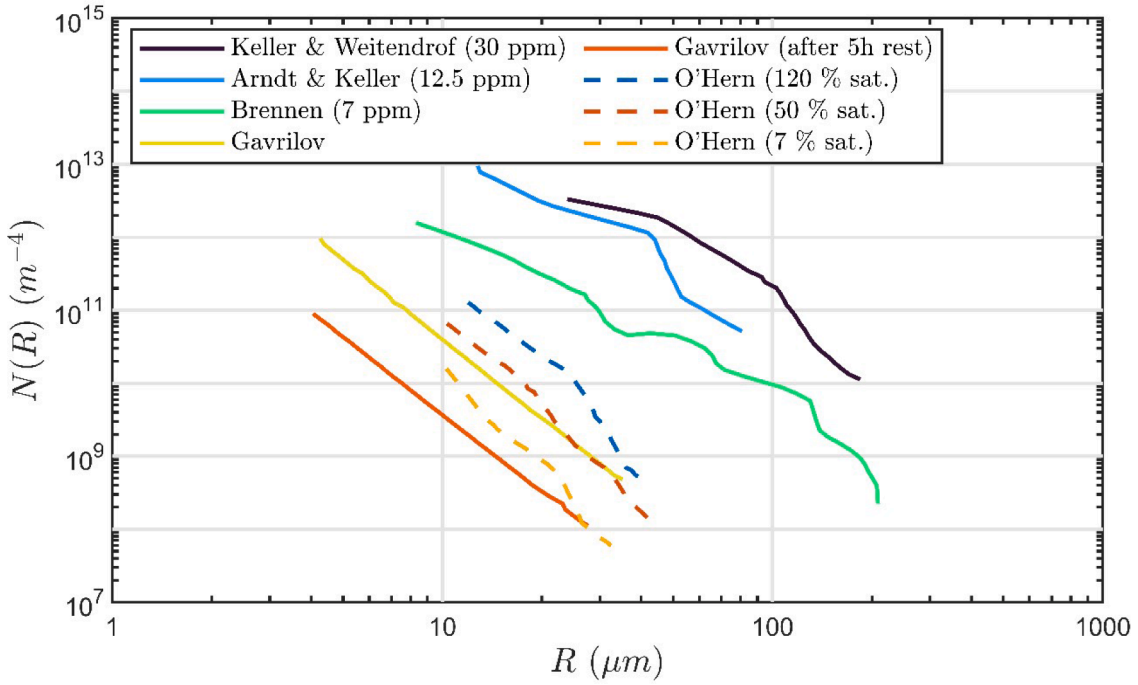

Fig. 1. Examples of bubble population data obtained using holography (dashed lines) and light scattering (continuous lines).

$$\alpha = \frac{\vartheta_{Bubbles}}{\vartheta_{\text{Liquid}} + \vartheta_{Bubbles}} = \frac{n \cdot \vartheta_B}{1 + n \cdot \vartheta_B} = \frac{n \frac{4}{3}\pi R_{30}^3}{1 + n \frac{4}{3}\pi R_{30}^3} \tag{16}$$

Where the volumetric average radius R_{30} is used as the most representative measure of mean bubble size. This formulation of the vapour volume fraction taken from (Sauer, 2000) allows to bound $\alpha \in [0, 1)$ without the need for additional numerical bounds and corrections which would otherwise be mandatory if a realistic solution is to be attained (Chebli et al., 2021).

2.4. Cavitation source term

The cavitation source term for the vapour transport equation in a mixture model is written as (Singhal et al., 2002):

$$S_{cav} = -\frac{\rho_B}{\rho_T}\frac{D\rho_T}{Dt} \tag{17}$$

Using the definition for ρ_T from (1) and applying partial differentiation, the term is developed:

$$S_{cav} = \frac{\rho_B}{\rho_T}\left(\underbrace{(\rho_L - \rho_B)\frac{D\alpha}{Dt}}_{\text{Bubble growth term}} - \underbrace{\alpha\frac{D\rho_B}{Dt}}_{\text{Compressibility term}} \right) \tag{18}$$

The bubble growth term is inherent to any Rayleigh-Plesset based cavitation model, while compressibility only applies for multiphase bubbles or simulations including temperature variations, although it is commonly neglected even in those cases. Using implicit differentiation, the differential in the bubble growth term is rewritten as:

$$\frac{D\alpha}{Dt} = \frac{D\alpha}{DR_{30}}\frac{DR_{30}}{Dt} = \frac{n4\pi R_{30}^2}{\left(1 + n\frac{4}{3}\pi R_{30}^3\right)^2}\frac{DR_{30}}{Dt} \tag{19}$$

And the link between the Eulerian frame of S_{cav} and the Lagrangian bubble motion modelled by the Rayleigh-Plesset equation is established through the material derivative DR_{30}/Dt, calculated using (9). The bubble pressure p_B is not constant but is assumed to change with radius following a polytropic expansion (Franc, 2007), hence being expressed as:

$$p_B = p_V + p_G = p_V + p_{G,0}\left(\frac{R_0}{R}\right)^{3\gamma} \tag{20}$$

with $p_{G,0}$ being a boundary condition depending on the initial volumetric mean bubble radius $R_{30,0}$:

$$p_{G,0} = p_{ref} - p_V + \frac{2\mathscr{S}}{R_{30,0}} \tag{21}$$

Where p_{ref} stands for the reference absolute pressure, which in the cases depicted in Fig. 1 is equivalent to atmospheric pressure. Under these assumptions and neglecting bubble compressibility, the cavitation source term is written as:

$$\begin{cases} S_{cav} = \dfrac{\rho_L \rho_B\ n4\pi}{\rho_T\left(1 + n\frac{4}{3}\pi R_{30}^3\right)^2}\left(-\dfrac{4\mu_L}{3\rho_L}R_{30} + \text{sign}(\varphi)\sqrt{|\varphi|}\right) \\ \varphi = \dfrac{2}{3}\dfrac{p_{G,0}}{\rho_L}R_{30,0}^{3\gamma}R_{30}^{4-3\gamma} + \dfrac{16\mu_L^2}{9\rho_L^2}R_{30}^2 - \dfrac{4\mathscr{S}}{3\rho_L}R_{30}^3 + \dfrac{2R_{30}^4}{3\rho_L}(p_V - p_\infty) \\ \rho_B = \rho_V + \rho_G = \ \rho_V + \rho_{G,0}\left(\dfrac{p_G}{p_{G,0}}\right)^{\gamma} = \ \rho_V + \dfrac{p_{G,0}}{K_G\ T}\left(\dfrac{R_{30,0}}{R_{30}}\right)^{3\gamma^2} \\ R_{30} = \left(\dfrac{\alpha}{1-\alpha}\ \dfrac{3}{4\ \pi\ n}\right)^{\frac{1}{3}} \end{cases} \tag{22}$$

where the fluid properties are treated as model constants, and their magnitude is evaluated at saturation conditions in accordance with the assumptions of the Rayleigh-Plesset equation (Plesset, 1949).

If this source term is applied to simulate the behaviour of a single bubble subjected to a known pressure field, the results obtained exhibit significant improvement with respect to the Rayleigh equation in (10) when compared to the full Rayleigh-Plesset equation. This is demonstrated in Fig. 2 in which a bubble with an initial size of $R_0 = 30\ \mu$m is subjected to a sinusoidal pressure drop falling below the vapour pressure of $p_V = 2350$ Pa, the nondimensional time evolution of radius being plotted in the left axis and that of the far-field pressure in the right axis.

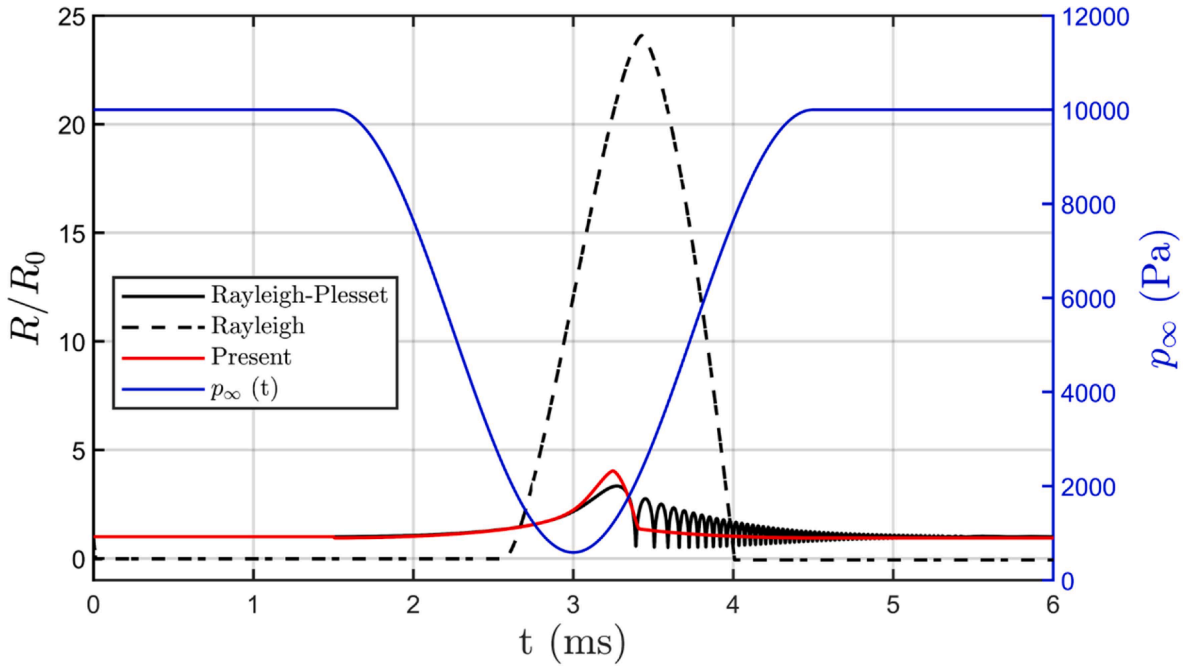

Fig. 2. Source term comparison for a single bubble subjected to a sinusoidal pressure drop.

While the Rayleigh equation clearly overestimates bubble growth, reaching a maximum radius of 24.1 R_0 when the Rayleigh-Plesset equation predicts 3.3 R_0, the expression in (22) leads to a much closer result of 4.0 R_0. A major improvement is also achieved in terms of collapse time accuracy, with the 3.4 ms calculated for the proposed model approaching much better the full Rayleigh-Plesset 3.3 ms than Rayleigh's 4.0 ms.

Moreover, the neglection of surface tension effects overlooks bubble equilibrium, and radius falls to zero unless $p_\infty < p_V$ while both the Rayleigh-Plesset equation and the present model agree in an $R = R_0$ equilibrium radius. When compared to the full expression, however, the source term in (22) neglects bubble oscillation after collapse. The inability to capture the multiple rebounds is due to the loss of the second order time derivative of bubble radius, which becomes highly negative during the collapse and in return increases the first order derivative according to (7) . This may be seen as a loss of accuracy, but it also represents an improvement in numerical stability as very fine meshes would be mandatory for proper calculation of these high-frequency rebounds; instead, the new source term provides a less demanding averaging of these fluctuations.

Regarding the compressibility term, time variation of bubble density is solely due to non-condensable gas content, and thus it can be

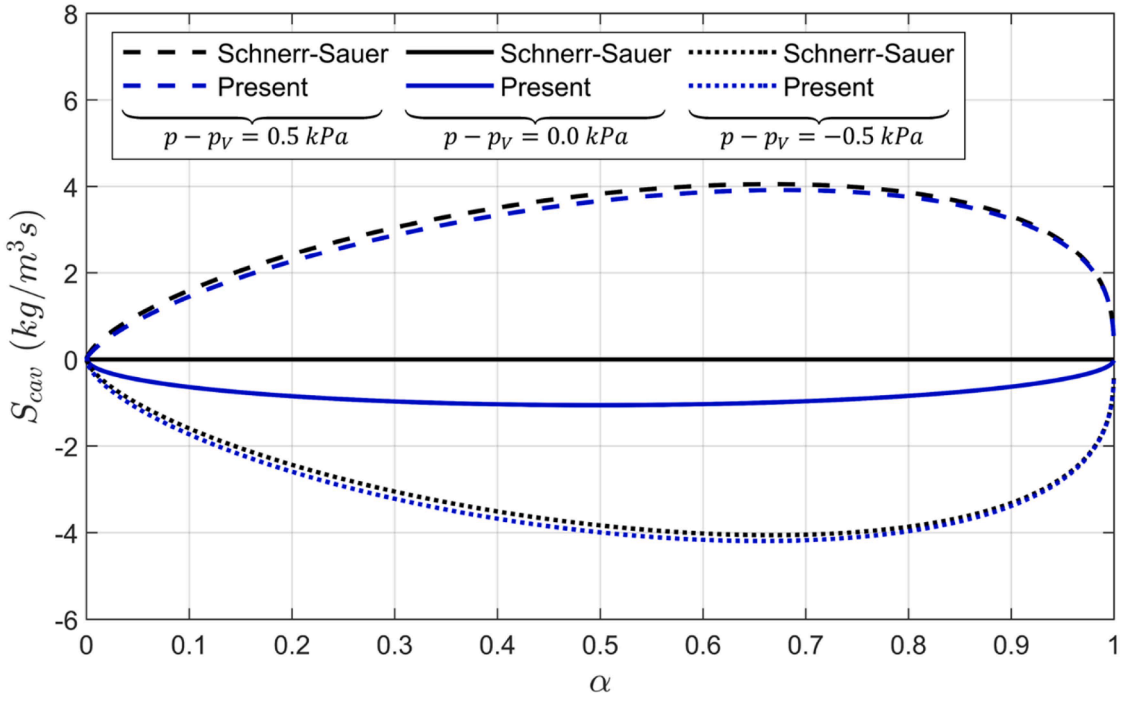

Fig. 3. Cavitation source term variation ($R_{30,0} = 8\ \mu m$) with pressure difference compared to Schnerr-Sauer model.

simplified as:

$$\alpha\frac{D\rho_B}{Dt}=\alpha\frac{D\rho_G}{Dt} \tag{23}$$

Which, using the expression for ρ_G given in (22) and applying the chain rule, yields:

$$\alpha\frac{D\rho_B}{Dt}=\alpha\ \rho_{G,0}\ R_{30,0}^{3\gamma}\ \frac{D\left(R_{30}^{-3\gamma}\right)}{Dt}=-\ \alpha\ \rho_{G,0}\ 3\gamma\ R_{30,0}^{3\gamma}\ R_{30}^{-3\gamma-1}\frac{DR_{30}}{Dt} \tag{24}$$

Where the differential term DR_{30}/Dt is substituted using (9) as done in (22).

Before proceeding to apply the slip velocity and turbulence corrections of the model, a comparison between the current source term and that of Schnerr-Sauer is provided in Fig. 3, where the magnitude of S_{cav} is plotted for three different far-field absolute pressures of 5 kPa, 0 kPa and −5 kPa relative to p_V as a function of the void fraction α. It shall be highlighted that the closer to zero the external pressure is, the lower the difference between source terms will be while their magnitude significantly differs near the vapour pressure. In addition, the present model preserves the numerically convenient boundedness between zero and one from which the Schnerr-Sauer model benefits.

2.5. Slip

Although the velocity of the bubbly phase $\vec{V}_{\vec{B}}$ (composed by a mixture of non-condensable gas and saturated vapour) appears in the vapour transport Eq. (6), it can be simplified under a no-slip assumption by considering that it is equal to the total flow velocity and bubbles strictly follow the pathlines described by the liquid as if they were massless particles. Although this results in an increased simplicity and time economy of the calculations, discrepancy with experimental results arises in many practical applications (Arabnejad et al., 2023). The absolute velocity of the bubbly phase can be written as the sum of the velocity of the liquid phase $\vec{V}_{\vec{L}}$ and the relative velocity of bubbles with respect to the liquid $\vec{V}_{\vec{B,L}}$:

$$\vec{V}_{\vec{B}}=\vec{V}_{\vec{L}}+\vec{V}_{\vec{B,L}} \tag{25}$$

The liquid velocity field is solved by means of the continuity equation, while the relative velocity $\vec{V}_{\vec{B,L}}$ is computed based on drag forces, gravity and turbulent diffusion following the Manninen et al. model (Maninnen et al., 1996):

$$\vec{V}_{\vec{B,L}}=\frac{16\ (\rho_B-\rho_T)R_{30}^2}{3\ \mu_L\ Re\ C_D}\left(\vec{g}^{\rightarrow}-\left(\vec{V}^{\rightarrow}\cdot\nabla\right)\vec{V}^{\rightarrow}-\frac{\partial\vec{V}^{\rightarrow}}{\partial t}\right)-\frac{\Gamma_t}{\sigma_t}\left(\frac{\nabla\alpha_B}{\alpha_B}-\frac{\nabla\alpha_L}{\alpha_L}\right) \tag{26}$$

Where the turbulent diffusivity Γ_t is calculated using the empirical correlation used by ANSYS FLUENT® when the $k-\varepsilon$ turbulence model is employed (ANSYS, 2024):

$$\Gamma_t=C_\mu\frac{k^2}{\varepsilon}\left(\frac{\gamma_\gamma}{1+\gamma_\gamma}\right)\frac{1}{\sqrt{1+\left(1.8-1.35\cos^2\left(\frac{\vec{V}_{\vec{B,L}}\cdot\vec{V}_{\vec{B}}}{V_{B,L}\ V_L}\right)\right)\ \frac{3\ k\ V_{B,L}^2}{2}}} \tag{27}$$

The drag coefficient for the bubbles (assuming a spherical shape) is computed following the Morsi-Alexander law (Morsi and Alexander, 1972). For computational stability reasons, a constant R_{30} is introduced in (26) as done in Arabnejad et al. (2023). On the one hand, as the magnitude of the slip velocity will only grow to a significant extent in zones where bubble size is greater, the average radius in these circumstances must forcedly exceed the initial volumetric average radius, $R_{30,0}$. On the other hand, the choice of a very large average radius will lead to an overprediction of the slip velocity effects. In the light of the above, the cavitation inception radius has been chosen as the most representative value for slip velocity calculation. Cavitation inception conditions correspond to the smallest visually spottable bubbles. Therefore, as the average human visual acuity corresponds to 0.1 mm (Levi, 2011), then the optical inception diameter is 100 μm and $R_{30}=100\ \mu m/2=50\ \mu m$ is introduced in (26).

The influence of turbulent diffusion and slip velocity on the final results of calculations will be discussed in the forthcoming sections.

2.6. Turbulence

The random velocity fluctuations characterizing turbulent flows also influence the pressure distribution in the fluid. For this reason, corrections based on empirically calculated probability density functions (Uberoi, 1953) have been used to correct the vapour pressure of fluids in order to account for the effects of pressure decrease below its average value (Singhal et al., 2002):

$$p_V^{turb}=p_V+p_V^{corr}(k) \tag{28}$$

These corrections commonly use the root mean square difference (equivalent to the standard deviation) to quantify the amplitude of these fluctuations, which have been observed to cover a wider range of pressures below than above the average. More recently, however, the work of Bappy et al. (2020) has revealed that these probability density distributions can be shifted towards even lower pressures as a result of the interaction with bubbles in the flow, i.e. an interaction takes place in which the presence of nuclei increases turbulence that, in turn, decreases the pressure and enhances nuclei growth. The ratio of bubble size with respect to the Taylor microscale is the governing parameter chosen to quantify the increase in the standard deviation promoted by nuclei presence.

Fig. 4.a adapts some of the data from Bappy et al., where the probability density function $p(P-\overline{P})$ is plotted for different values of pressure difference above and below the mean non-dimensional pressure $\overline{P}$. It can be seen that the probability density of lower pressures increases at nuclei sizes which are greater with respect to turbulent eddies. A shift from the initial average pressure is also observed, and hence the correction to be applied must take into consideration both *shifting* and *widening* effects of the function:

$$p_V^{corr}(k,\varepsilon)=\frac{2k_{\rho_L}}{3}\left(\underbrace{\Delta\overline{P}^{'}}_{\text{Shifting}}-\underbrace{\frac{1}{2}\mathbf{P}^{'}_{RMS}}_{\text{Widening}}\right) \tag{29}$$

Fortunately, Bappy et al. provide straightforward correlations for both terms as a function of the Taylor microscale λ and a buoyancy parameter w:

$$\begin{cases}\lambda=\sqrt{10k/\varepsilon}\\ w=\dfrac{2gR_{30}^2}{9\nu_L\sqrt{3k/2}}\end{cases} \tag{30}$$

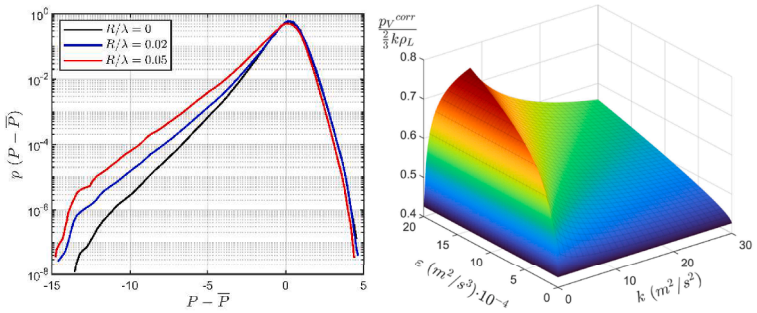

(a) (b)

Fig. 4. Turbulent pressure probability density function for different bubble radii (a) at $\boldsymbol{w}\rightarrow 0$ and vapour pressure correction term variation with turbulence (b).

The developed form of these correction terms is:

$$\begin{cases} \Delta\overline{P'} = \left(75\left[\min\left(\frac{R_{30}}{\lambda}, 0.05\right)\right]^2 + 2\min\left(\frac{R_{30}}{\lambda}, 0.05\right)\right)e^{-\frac{1}{2}w} \\ P'_{RMS} = \left(0.725 + 150\left[\min\left(\frac{R_{30}}{\lambda}, 0.05\right)\right]^2 e^{-\frac{1}{2}w} + 3.75\min\left(\frac{R_{30}}{\lambda}, 0.05\right)e^{-\frac{1}{2}w}\right)^{\frac{1}{2}} \end{cases} \tag{31}$$

The nondimensional correction of vapour pressure is represented in Fig. 4.b as a function of the parameters involved in the $k-\varepsilon$ model for a constant bubble size of 1 mm. Although the usual value of p_V^{corr} in absence of turbulence-bubble interaction is 0.43, maxima above 0.75 are obtained when considering this correction in the range under study. Generally, higher dissipation rates lead to increased turbulence-corrected vapour pressure.

3. Validation Methodology

The developed model is coupled to the commercial CFD suite ANSYS® FLUENT by means of four User-Defined Functions (UDFs) programmed in C++ code, namely: source term, bubbly phase density, bubble diameter for slip velocity calculation and compressibility correction for the turbulence model. A first-order time-implicit formulation is chosen for the cavitation source term combined with an explicit algorithm to be solved in each iteration inside the same time step. First order upwind is used for the convective term the vapour transport equation as recommended by Schnerr and Sauer (2001), while second order upwind is preferred for momentum and turbulence equations. The equation system is solved using a PISO scheme (Issa et al., 1986) to reduce the timestep requirements for convergence, and relaxation factors of 0.7 and 0.3 are respectively used in the momentum and continuity equations. A stronger criterion is used for the vapour transport equation, forcing a 0.1 relaxation factor for the cavitation source term and the slip velocity while a milder 0.3 in void fraction is enough to ensure stability.

3.1. Validation case

Experimental results by Sou et al. have widely been used to validate and assess the performance of cavitation models for in-nozzle flow behaviour and jet atomization (Trummler et al., 2020). In the present work, jet atomization is being left aside in favour of convergent-nozzle behaviour evaluation taking Sou et al.'s 2D symmetric nozzle experiment (Sou et al., 2007) as the benchmark for this analysis. The geometry of the experimental setup is depicted in Fig. 5, showing a symmetric

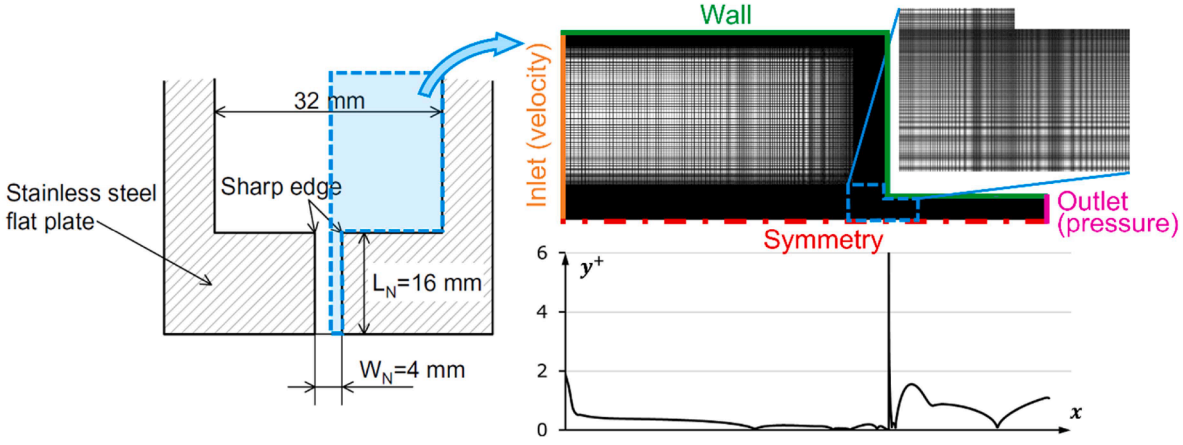

Fig. 5. Experimental setup from Sou et al. (reproduced from Sou et al. (2007)) and computational mesh.

Table 1
Case studies for the validation using Sou et al.'s injector nozzle.

Case	Reynolds number, Re	Cavitation number, σ
1	$5.0{\cdot}10^4$	1.27
2	$5.8{\cdot}10^4$	0.95
3	$6.4{\cdot}10^4$	0.78
4	$7.0{\cdot}10^4$	0.65

Table 2
Model constants used in Eq. (22).

Variable	Symbol	Magnitude
Liquid density	ρ_L	998.2 kg/m^3
Saturated vapor density	ρ_V	0.017 kg/m^3
Liquid dynamic viscosity	μ_L	$1.002{\cdot}10^{-3}$ $Pa{\cdot}s$
Isentropic expansion coefficient	γ	1.4
Surface tension at the liquid-vapor interface	$\mathscr{S}$	0.073 N/m
Vapor pressure	p_V	2353 Pa
Working temperature	T	293 K
Gas constant of air	K_G	287 $J/kg\,K$
Initial average volumetric radius	$R_{30,0}$	8 μm
Bubble number density	n	$5{\cdot}10^6$ m^{-3}

nozzle with an 8:1 area reduction and a throat length of 16 mm with a constant depth of 1 mm. As the nature of the experiment is clearly two-dimensional, 2D numerical simulations will be carried out along the validation process together with the simplification of midplane symmetry. A prescribed normal velocity is used as the inlet boundary condition, while pressure outlet is applied to ensure atmospheric conditions at the throat end. The outlet void fraction is set to zero while the inlet void fraction is calculated from the O'Hern 7 % nuclei distribution in Fig. 1 yielding $n = 5{\cdot}10^6\ m^{-3}$ and $R_{30,0} = 8\ \mu$m. This is considered to be a representative measure of the working fluid used by Sou et al., who claim to have used distilled and filtered water in their experiments to reduce initial nuclei population as much as possible.

A cartesian structured mesh is used, featuring thorough refinements near walls and increased cell number in the throat section (especially near the sharp edge). The longitudinal distribution of wall y^+ is also plotted in Fig. 5, in which a maximum value of 6 is attained at the front wall while the side walls of the throat and chamber fulfil that $y^+ < 2$; this allows to use an enhanced wall treatment that significantly improves the capabilities of the $k-\varepsilon$ model. A constant time step $\Delta t = 0.5\ \mu s$ is used, yielding an average Courant number of 0.034 with a maximum of 3.37. The convergence criterion requires the nondimensional residuals for void fraction, pressure, velocity, turbulent kinetic energy and dissipation rate to fall below $1{\cdot}10^{-5}$, no variation in the solution being observed below $1{\cdot}10^{-4}$. At least five cavity shedding cycles are simulated in each working point to ensure that a periodic solution is achieved.

Following Sou et al.'s experimental campaign, four working points characterized by their cavitation number σ are analysed, each of them characterized by a variable Reynolds number Re as detailed in Table 1. As the outlet pressure is kept at atmospheric conditions, the cavitation number is reduced by increasing the inlet velocity and thus the Re.

The model constants used in (22), related to the properties of the working fluid, are summarized in Table 2. Physical and thermodynamic fluid properties are evaluated in saturation conditions at the working temperature of 293 K according to Sou et al. (2007).

3.2. Mesh sensitivity

A mesh sensitivity study based on velocity, turbulent kinetic energy and void fraction is carried out to ensure mesh independence of the validation results. For this purpose, a steady-state solution of Case 3 is computed and the velocity and turbulent kinetic energy profiles at the throat section are measured together with the average volume fraction $\overline{\alpha}$ in the domain. Five computational grids with increasing cell number are used to estimate the overall discretization error according to the Grid Convergence Index method proposed by Roache (1994) based on Richardson extrapolation. The mesh h_4 featuring an average cell size of 32 μm with a total count of $2.7{\cdot}10^3$ cells has been chosen attending to a grid convergence index of 1.18 % computed based on the $\overline{\alpha}$ for h_4, h_3 and h_2. The evolution of $\overline{\alpha}$ with mean cell size h is represented in Fig. 6, showing that no significant grid convergence advantage is gained by

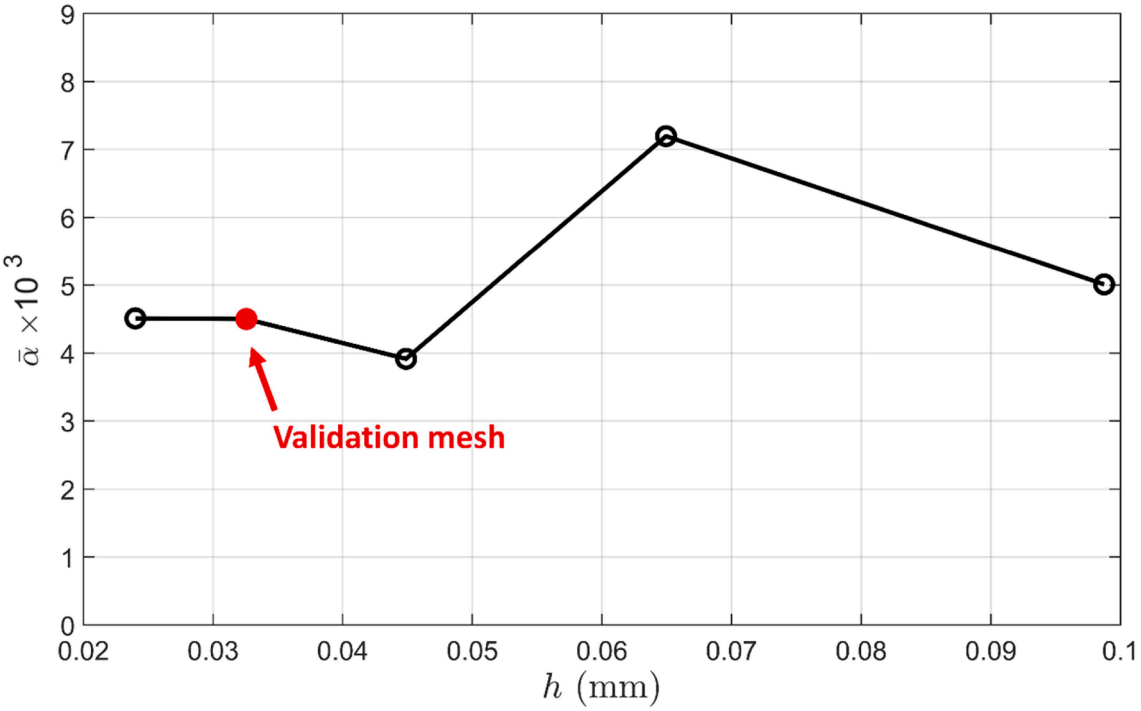

Fig. 6. Mesh sensitivity study based on the average α in the domain.

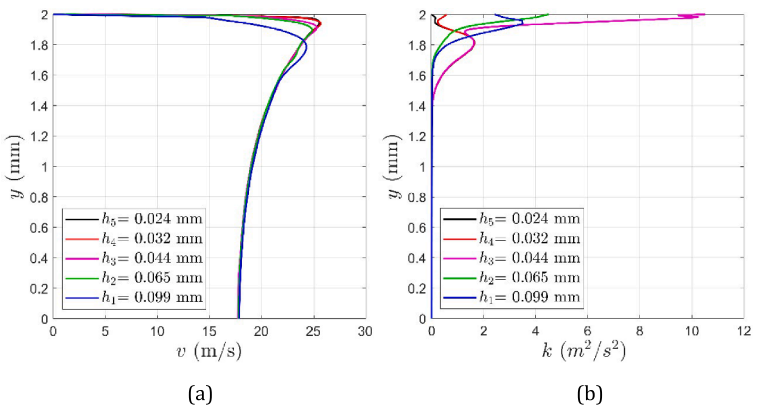

Fig. 7. Mesh sensitivity study of velocity (a) and turbulent kinetic energy (b) profiles at the nozzle throat.

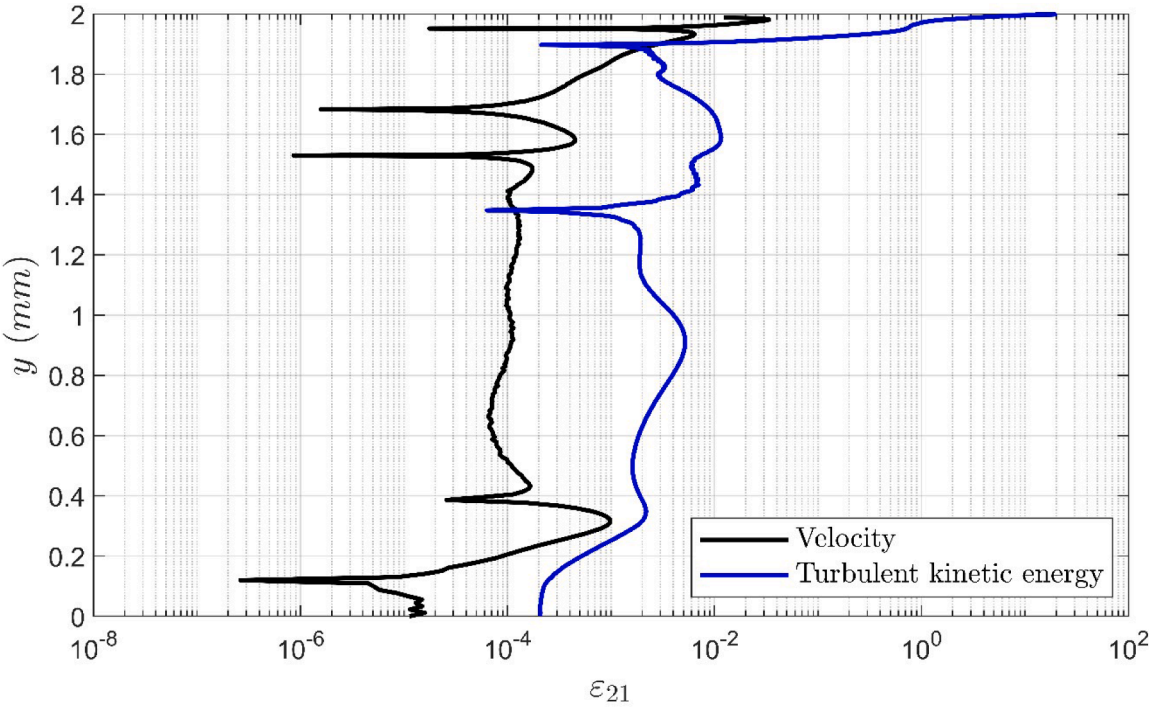

Fig. 8. Relative grid convergence error in the velocity and turbulent kinetic energy profiles for the final mesh.

further refining the mesh.

Grid convergence is confirmed by the evolution of velocity and turbulent kinetic energy profiles at the throat section depicted in Fig. 7. Although lagging with respect to velocity, k does converge as well and the relative error ε_{21} profile for both variables is kept below 1 % as shown in Fig. 8. Although increased relative error is obtained near $y =$ 2 mm as a result of both profiles tending to zero, mesh convergence in this zone can be checked in Fig. 7.

4. Results and discussion

Model validation is based on the comparison between numerical and experimental results that allow to evaluate the accuracy with which the proposed model is able to reproduce cavity morphology and unsteady dynamics. A discussion on the influence of compressibility and slip velocity terms is provided in first place, followed by a comparison of void fraction contours at different cavitation numbers with their experimental counterparts in Sou et al. (2007). A bubble population sensitivity analysis is also conducted. A comparison between the obtained results and those predicted by Lagrangian Rayleigh-Plesset single bubble dynamics is provided so as to show the ability of the model to reproduce not only macroscopic, but also microscopic flow features holding considerable interest for cavitation inception studies. Finally, the influence of the turbulence modelling approach is studied by means of a comparison between the results obtained from URANS and Detached Eddy Simulation (DES) calculations using both the Schnerr-Sauer and the proposed model.

4.1. Influence of compressibility and slip terms

Taking Case 3 as the benchmark working point, simulations including and neglecting both compressibility (Eq. (18)) and liquid-bubble slip (Eq. (26)) have been carried out in order to perform a sensitivity study that allows to quantify the influence of such model improvements. Fig. 9 compares the time evolution of average vapour volume fraction in the nozzle for the three alternatives studied along one complete cavity shedding cycle (once a periodic regime has been reached). As expected, the inclusion of compressibility effects in the full

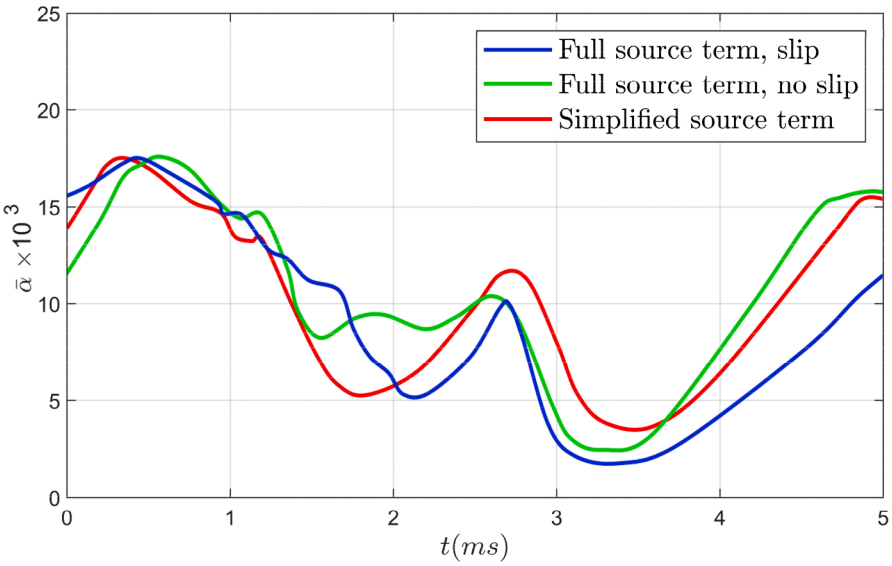

Fig. 9. Time evolution of average α in the nozzle throat using different source terms.

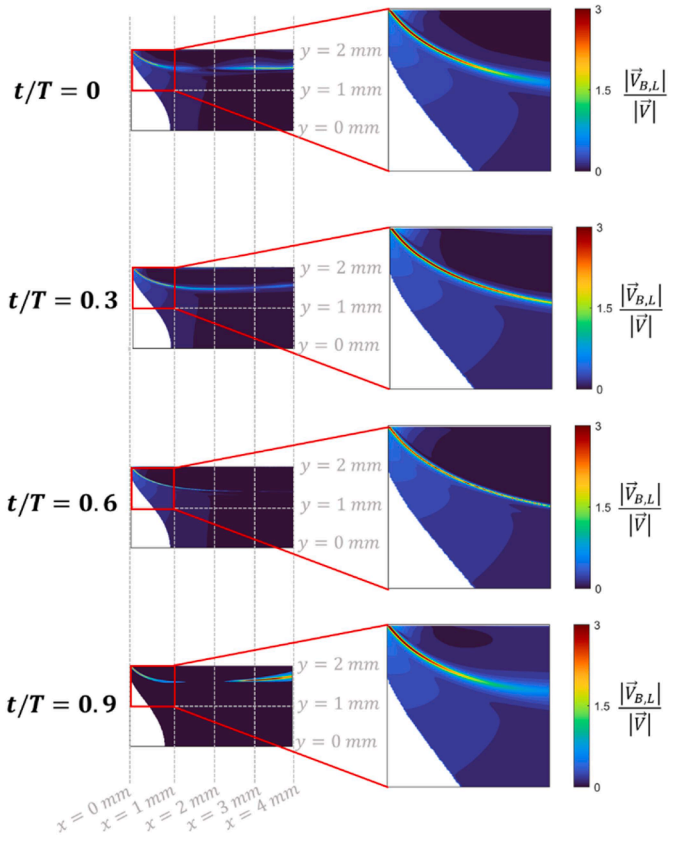

Fig. 10. Normalized bubble slip velocity magnitude in the nozzle.

source term (green curve) does not imply a drastic change regarding cavity dynamics when compared to the baseline simplified source term (red curve), although a slight reduction in the cavity growth rate can be perceived as the slope of the α vs. t evolution experiences an increase after the cavity shedding point near $t = 3$ ms. When slip effects are considered (blue curve), however, the growth rate is reduced but the general shape of the void fraction time variation is maintained. In the light of the above, the three models present a remarkable similarity that allows to neglect slip and non-condensable gas compressibility without any noticeable detriment to accuracy. A common shedding frequency around $f = 1/T = 200$ Hz is obtained, in accordance with experimental data and the RANS simulations from Biçer and Sou (2016).

Although its influence has been proven to be negligible, a further analysis of the influence of slip velocity is conducted so as to provide further insight on the underlying flow phenomena. For this purpose, the vapour velocity contours at different time steps t/T are shown in Fig. 10. The relative bubble velocity modulus normalized with respect to that of the total velocity is represented in the colour scale, especially focusing on closest zone to the nozzle sharp edge in which the majority of the slip phenomena are taking place. A clear increase of the slip velocity magnitude is identified at the liquid-vapour interface, with slip velocity magnitudes reaching three times the modulus of the global flow speed. The black dashed line represents the activation threshold of the slip velocity formulation, meaning that in the white are the bubble size is small enough for perfect bubble-liquid velocity coupling to be acceptable (this does imply, however, that the void fraction α is null). If the slip velocity magnitude contours are compared at different time steps only minor differences arise, being due to the changes in the cavity shape resulting from the unsteady nature of the flow under study.

If the direction (and not only the magnitude) of the relative velocity is also monitored as done in Fig. 11, in which blue areas correspond to bubble slip opposite to the global flow and red zones denote relative motion in favour of the global velocity field, relevant flow features regarding the flow acceleration identified in Fig. 10 arise. On the one hand, strong positive slip in the liquid side of the interphase can be spotted in both the x and y components. On the other hand, the vapour side of the interphase is characterized by negative slip opposing the global flow direction. Even though the slip velocity magnitude does not experience relevant variations with flow unsteadiness, its vectorial components do change along the cavity shedding cycle (especially in the y direction), giving rise to an interaction between the slip and phase change mechanisms near the nozzle edge. The extent of this interaction attending to Fig. 9, however, is weak due to the low magnitude of the y velocities, especially inside the cavity where flow recirculation is the governing phenomenon. For this reason, and even though its introduction may be interesting for the study of detailed flow features, slip velocity can be considered negligible for the current case.

As for the compressibility term, no major influence on global flow behaviour is observed and therefore it can be considered negligible. Careful inspection of (18) reveals that the density derivative $D\rho_B/Dt$ only has a relevant magnitude with respect to the phase change term when the pressure outside the bubbles is above p_V. This situation cor-

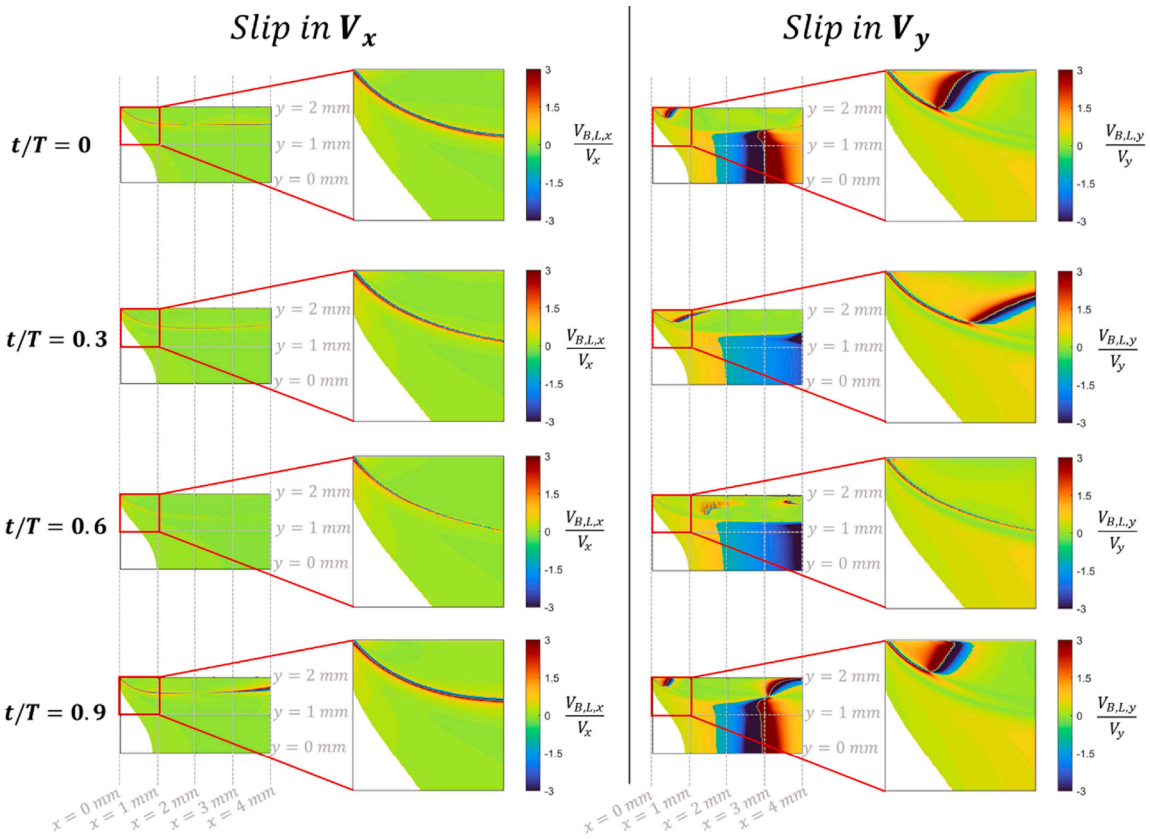

Fig. 11. Normalized x and y components of bubble slip velocity.

responds to a reduced bubble diameter $R \approx R_0$ as a result of which α is very small and therefore contributes to cancel the relevance of the $\alpha D\rho_B/Dt$ term.

4.2. Comparison with experimental results

The validation of the presented model is carried out by means of a comparison with both the experimental results by Sou et al. and the calculations performed using the Schnerr-Sauer source term. In all the cases under study, the proposed model is able to predict the unstable cavity behaviour while the Schnerr-Sauer formulation cannot, instead delivering a steady solution even for unsteady calculations.

At the working point corresponding to $\sigma = 1.27$, both the Schnerr-Sauer and the proposed model succeed at predicting no cavity formation on the nozzle walls (Fig. 12). At a lower $\sigma = 0.78$ corresponding to moderate cavitation, however, significant improvements with respect to the Schnerr-Sauer formulation is observed in Fig. 13. One major difference between both models arises in the formation of a re-entrant that compromises cavity stability and promotes the characteristic shedding dynamics described at different time steps t/T where T is the cavity shedding period (this period, although constant for each working point, changes slightly with σ). The Schnerr-Sauer model is unable to reproduce these dynamics, and the cavity morphology remains unchanged once a stable regime is reached. For this reason, the time evolution of the α contours is not shown for the Schnerr-Sauer solution as it would not provide further insight on the comparison. The neglection of the re-entrant jet, together with the inherent overestimation of bubble growth that was already identified in Fig. 2, lead the Schnerr-Sauer model to overestimate cavity length while the more conservative proposed model is able to accurately predict the cavity endpoint ($t/T = 0$ and $t/T = 0.9$). At $t/T = 0.3$, the shedding of a microbubble from the cavity can be spotted, leading to an increased unsteadiness at $t/T = 0.6$ characterized by the formation of a series of re-entrant jets impinging the cavity interphase until final stabilization is attained at $t/T = 0.9$.

At $\sigma = 0.78$, the time evolution of the void fraction contours can be tracked at different nozzle planes to show the improvements with respect the Schnerr-Sauer formulation. This is possible thanks to Fig. 14, in which three locations (corresponding to $x = 1\ mm$, $x = 5\ mm$ and $x = 10\ mm$) have been chosen to monitor the vertical evolution of the α contours in Fig. 13. The results obtained by the Schnerr-Sauer model are depicted in black, dashed lines while the solid lines show the outcome of the calculations performed applying the proposed model, with a colour scale representing the non-dimensional time. As the x coordinate of the planes advances towards the nozzle outlet, it can be observed that the cavity width increases while the maximum void fraction decreases. The effect of the re-entrant jet is also shown in the results obtained by means of the proposed model, the void fraction near the walls being lower than the one calculated near the cavity interface. This effect is not reproduced by the Schnerr-Sauer contours, for which the void fraction exhibits a strictly increasing monotonicity when approaching the walls in contrast with the experimental evidence of re-entrant jet presence.

If the cavitation number is further reduced to $\sigma = 0.65$, the longer, more stable cavities observed in Sou's experiments are also faithfully reproduced by the new model (Fig. 15) while the Schnerr-Sauer simulation fails at predicting the sharp cavity endpoint and the vapour-free recirculation areas close to the nozzle walls. It shall be remarked that flow unsteadiness is minimum in these conditions, and complete shedding does never take place with the cavities changing size but never condensing. These tendencies are replicated if the void fraction contours in Fig. 16 are analysed. It should be noted that the differences at variable non-dimensional time t/T are reduced with respect to the $\sigma = 0.78$ case, and the re-entrant jet is once again captured by the proposed model while the Schnerr-Sauer formulation still provides a strictly increasing monotonicity of α near the nozzle wall.

Finally, a phenomenon known as *hydraulic flip* was observed at $\sigma = 0.55$ during the experimental campaign by Sou et al., consisting on the

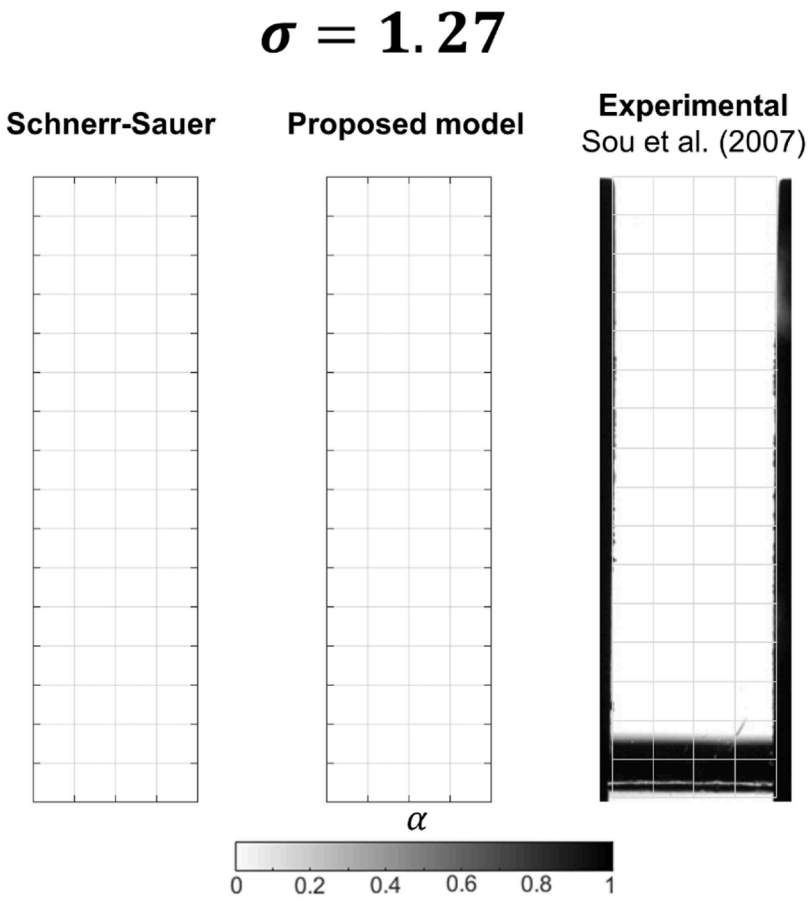

Fig. 12. Cavity evolution at $\sigma = 1.27$.

unsteady formation and condensation of cavities on alternative sides of the injector leading to flow asymmetry at low cavitation numbers. In order to test the ability of the current model to replicate the aforementioned flow features, the mesh symmetry in Fig. 5 is undone and the full 2D injector is used as the calculation domain. Although flow symmetry still does hold during the first five shedding cycles, increased turbulence caused by the previously described re-entrant jet soon leads to an asymmetry that is maintained throughout the subsequent cycles. The void fraction contours arising from calculations using the proposed model are depicted in Fig. 17, where the transition from a symmetric regime at $t/T = 0$ to a fully developed hydraulic flip at $t/T = 0.9$ can be traced. The cavity length, however, is not replicated as accurately as for the $\sigma = 0.65$ and $\sigma = 0.78$ cases except for the $t/T = 0.6$ time step in which cavities span along the full length of the nozzle. This alternating behaviour is clearly visible in Fig. 18, in which the time evolution of the void fraction contours is depicted. An evident asymmetry arises between the α levels at positive and negative magnitudes of the y coordinate. The unsteady nature of the phenomenon is highlighted by the fact that this asymmetry is inverted at different time steps. For instance, at $x = 10$ *mm* and $t/T = 0.3$, the void fraction reaches a maximum of $\alpha = 0.18$ in the positive (top) y coordinate, while no vapor phase is present in the negative (bottom) part. However, at $t/T = 0.9$, a maximum of $\alpha = 0.82$ is attained in the negative (bottom) y coordinate, while the maximum vapor presence in the top part of the graph is merely $\alpha = 0.02$.

From the analysis of the discussed results, it can be concluded that significant improvement with respect to the Schnerr-Sauer model has been attained at the macroscopic flow level. This is due to the high turbulence inherent to the near-wall nozzle flow, for which the proposed turbulence corrections represent a relevant enhancement. The more conservative nature of the presented phase change source term also corrects the overestimation of cavitation that penalizes the Schnerr-Sauer model at higher values of σ, while the accuracy of the cavity length prediction at lower cavitation numbers is also improved.

4.3. Sensitivity to bubble population

Recovering Case 3 as the benchmark for parametric variations, the sensitivity of the results to bubble populations can be studied. Two different parameters, namely the total bubble population n and the initial volumetric average bubble radius R_{30}, can be tuned in order to obtain different initial nuclei distributions. The effect of the total bubble count, however, is definitely trivial as the source term scales linearly with n (notice that, in (22), n appears both in the numerator and denominator but the latter is cancelled by the $n^{-1/3}$ present in the definition of R_{30}, which is raised to the third power). This property is not unique to the new model being presented, but a general rule in cavitation models instead. Changes in the initial bubble radius, however, do give rise to nonlinear variations as presented in Fig. 19. By increasing the initial bubble radius from 8 μm to 50 μm, a strong variation favouring cavitation inception at low α appears and alters the shape of the source term characteristics given by Fig. 3.

This inception proneness is translated to the numerical calculation of the injector flow, for which the results obtained at both values of $R_{30,0}$ are compared by means of Fig. 20, in which the cavity evolution under the greater $R_{30,0} = 50$ μm is plotted in orange colour to facilitate the comparison. As expected from the above discussion of Fig. 19, the increase in the initial bubble radius promotes a more severe cavitating regime; this is also in accordance with experimental results in other geometries (Pearsall, 1972), and allows to conduct a working-fluid-sensitivity test which may hold considerable interest in a wide range of applications such as turbomachinery flows. Despite the

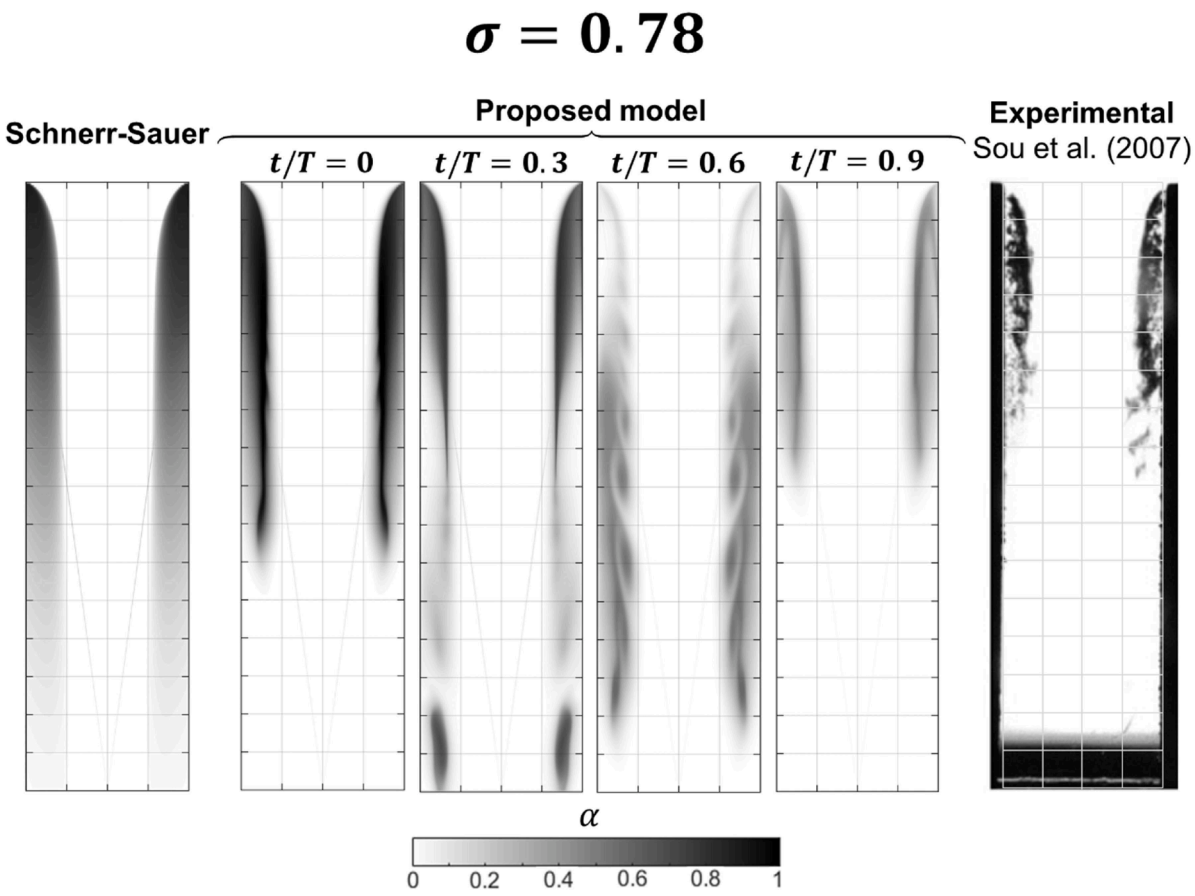

Fig. 13. Cavity evolution at $\sigma = 0.78$.

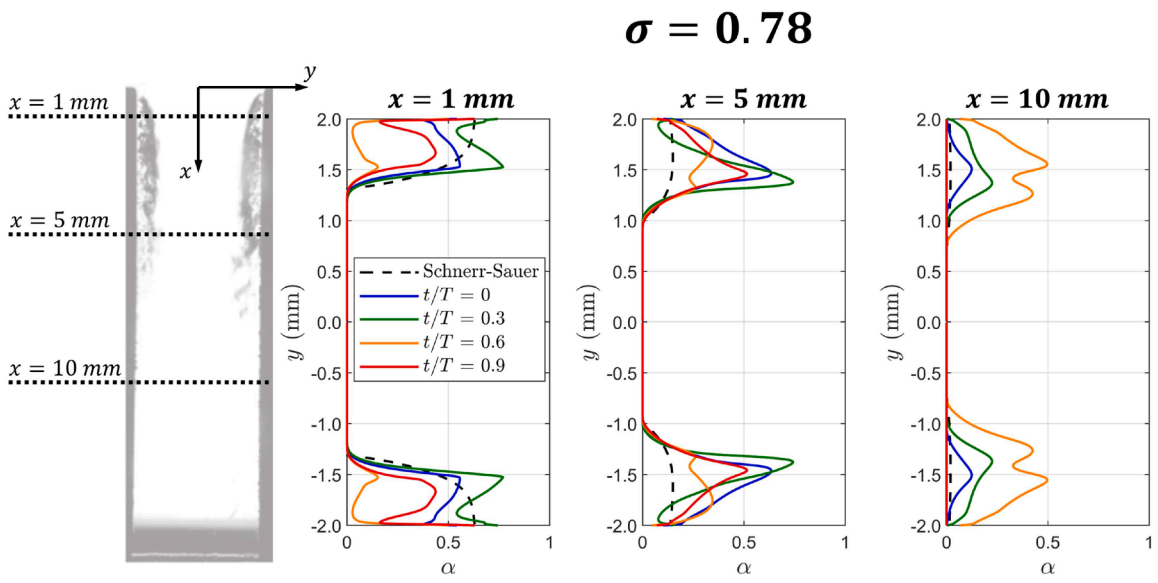

Fig. 14. Void fraction contours in selected planes at $\sigma = 0.78$.

similitude between the cavity morphologies observed at $t/T = 0$, the cavities corresponding to the higher initial radius consistently exhibit a longer span. At $t/T = 0.6$ it is also observed that the highly turbulent regime of re-entrant jets impinging the cavity no longer exists, being replaced by a more stable cavity instead; this leads to a faster recovery of the original morphology, and the length of the cavity at $t/T = 0.9$ is clearly greater than its $R_{30,0} = 8$ μm counterpart. As the working fluid used in the experiments by Sou et al. has a low non-dissolved air concentration and a small average nuclei size, the close agreement between numerical and experimental cavity morphologies is impoverished when

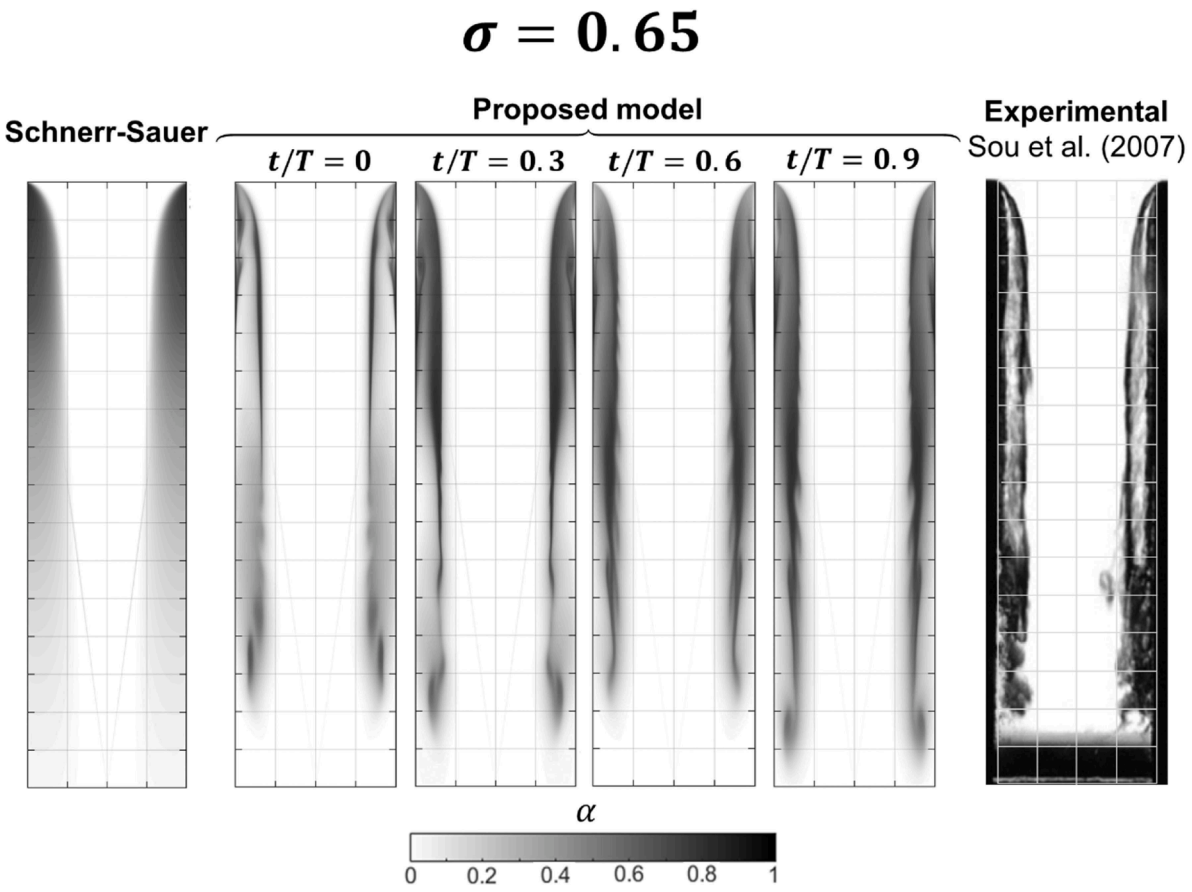

Fig. 15. Cavity evolution at $\sigma = 0.65$.

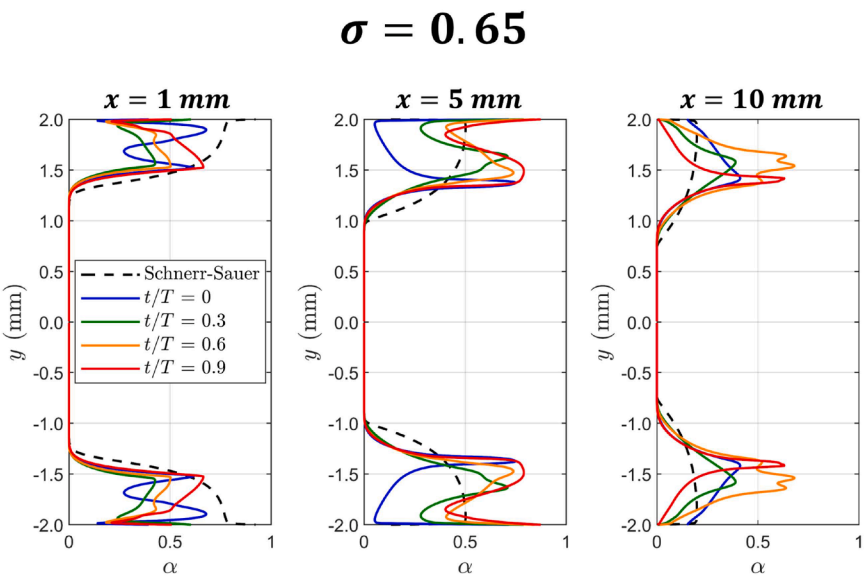

Fig. 16. Void fraction contours in selected planes at $\sigma = 0.65$.

increasing the initial bubble radius.

4.4. Microbubble behaviour

Although the present model is aimed at providing a more accurate description of bubble behaviour, the validation methodology has mainly focused on the study of void fraction instead of microbubble size. Once it has been checked that the proposed model is able to introduce significant improvements in the macro-features of the flow, the current analysis is concluded with an evaluation of its ability to reproduce the behaviour of single bubbles governed by the full Rayleigh-Plesset equation. For this purpose, the most critical flow pathline (i.e., that where the lowest pressure is attained) is extracted from the numerical calculations. The differential R-P equation is applied to the $p_\infty(t)$ pres-

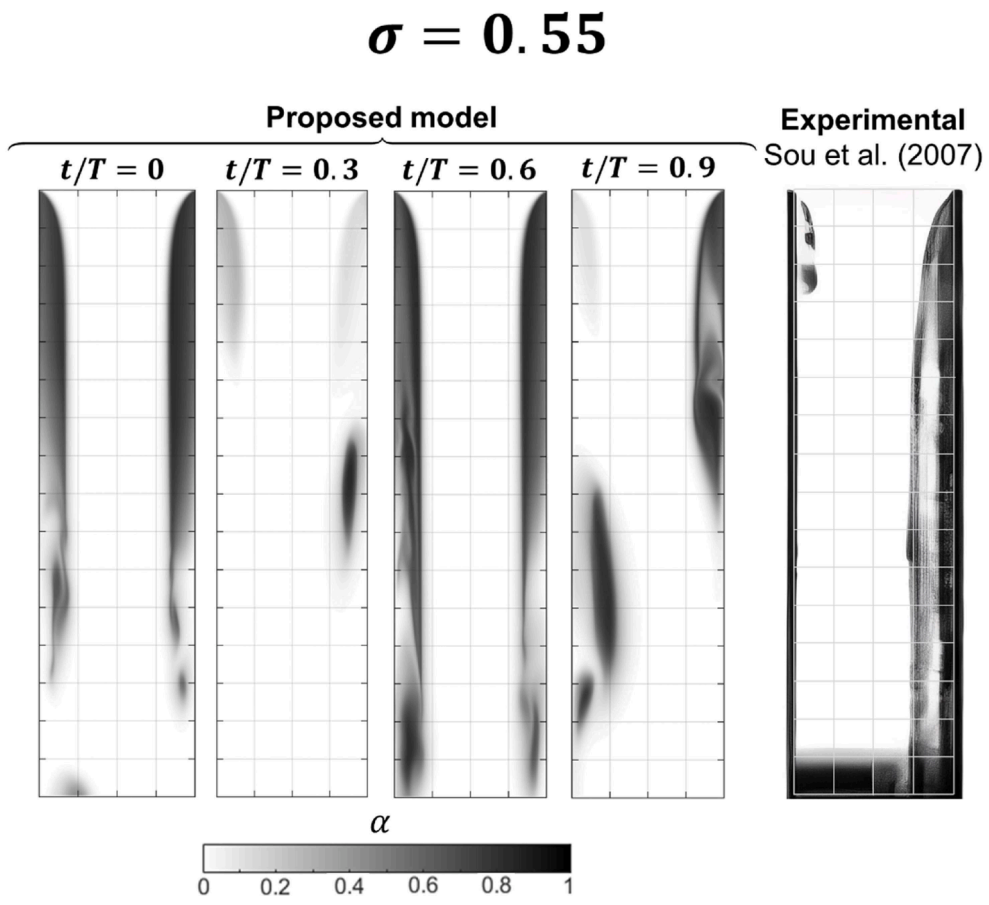

Fig. 17. Cavity evolution at $\sigma = 0.55$, showing hydraulic flip.

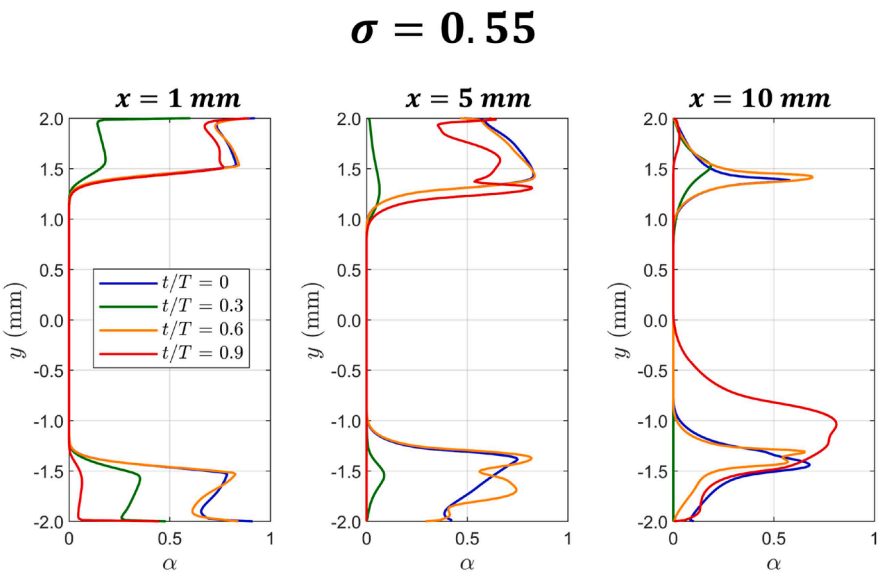

Fig. 18. Void fraction contours in selected planes at $\sigma = 0.55$.

sure history along this pathline in order to compare the obtained bubble size with that obtained from the $\alpha(t)$ history computed by means of the numerical model along the same pathline. In addition, the bubble size distribution computed by the Schnerr-Sauer model is also provided so as to allow a comparison with both the new model and the differential R-P results (which are given both for the static pressure history and for a corrected pressure given by Eq. (28)). Fig. 21 compares the pressure history (blue line) with the bubble size evolution given by the three aforementioned methods under analysis at $\sigma = 0.78$ (Fig. 21.a) and $\sigma = 0.65$ (Fig. 21.b).

At $\sigma = 0.78$, the Schnerr-Sauer model is unable to predict bubble presence because the static pressure along the pathline does never fall below p_V; consequently, a constant $R/R_0 = 0$ is obtained. The proposed model, however, accurately replicates the behaviour of the full

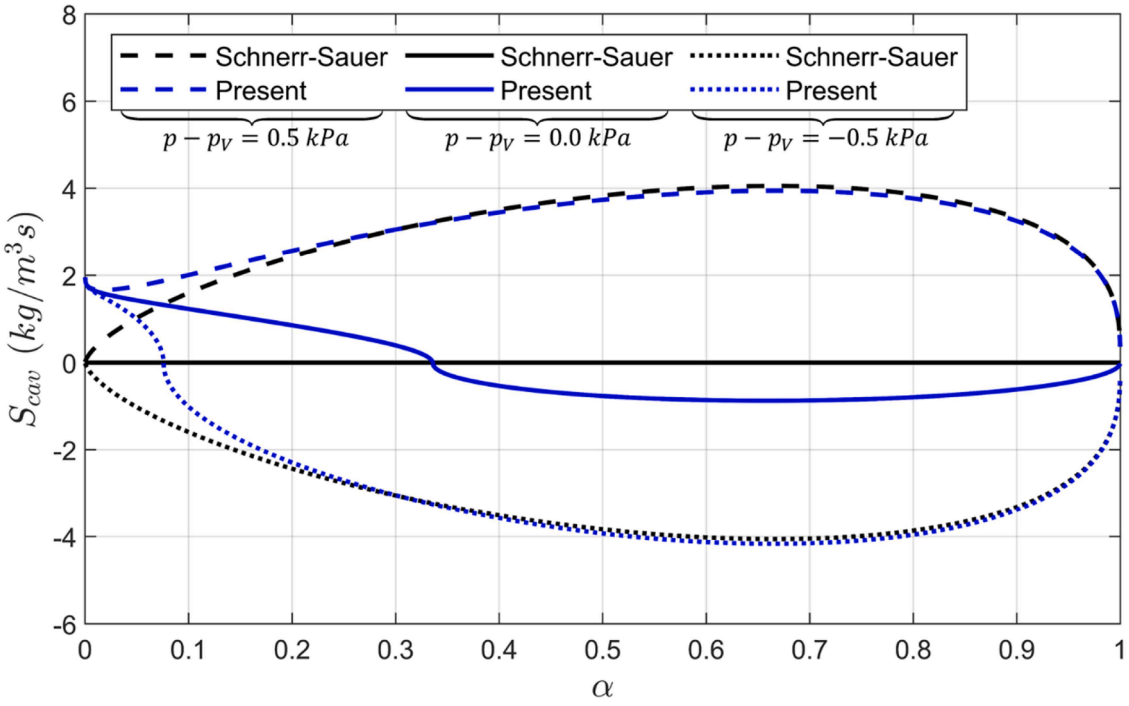

Fig. 19. Cavitation source term variation ($R_{30,0} = 50\ \mu m$) with pressure difference compared to Schnerr-Sauer model.

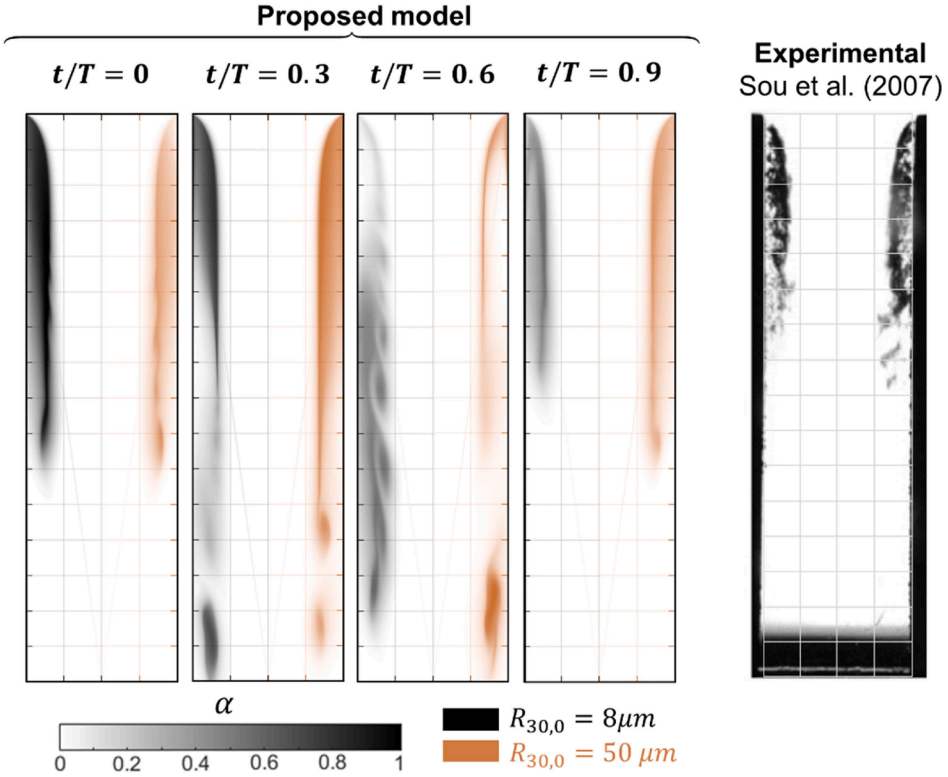

Fig. 20. Cavity morphology variation with increased initial bubble size at $\sigma = 0.78$.

Rayleigh-Plesset equation while the turbulence correction is not relevant in this case. Equilibrium effects are also captured by the proposed model, for which $R = 0$ is never obtained and the bubble size returns to $R/R_0 = 1$ as expected from the resolution of the full equation in differential form.

On the other hand, relevant differences between the models are observed at $\sigma = 0.65$. The uncorrected full R-P equation clearly underpredicts bubble size as happens with the Schnerr-Sauer model. If the turbulent correction is applied, however, the solution of the Rayleigh-Plesset differential equation approaches the CFD solution attained by means of the proposed model. This discrepancy between the red, continuous and black, dashed curves is due to the 2D convective

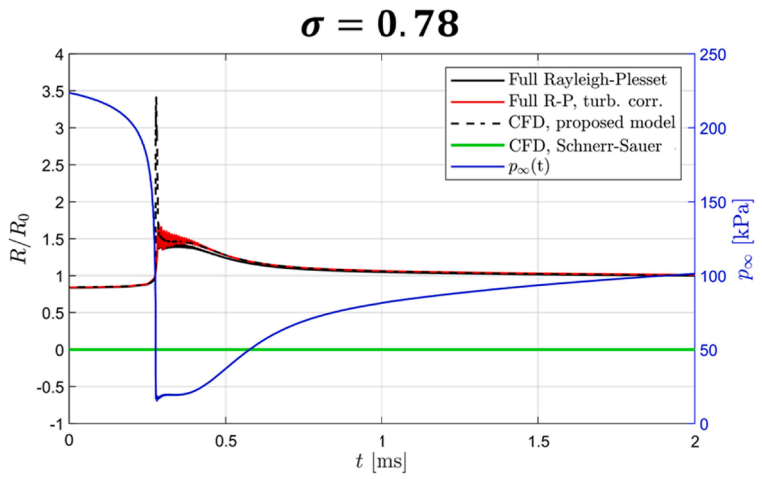

(a)

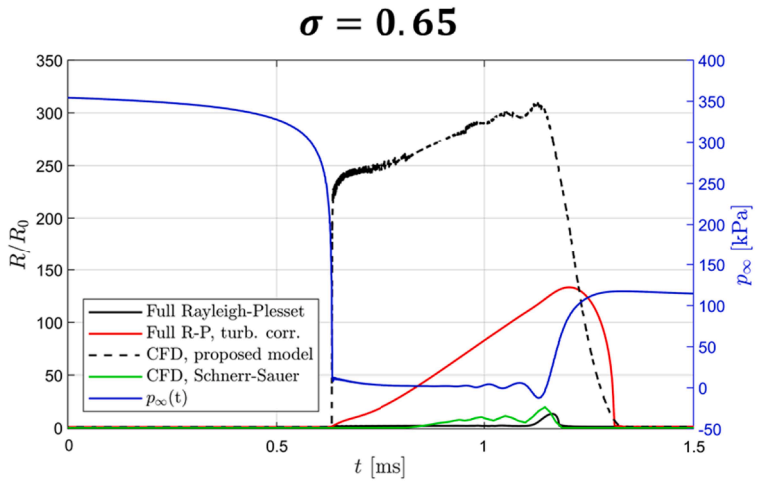

(b)

Fig. 21. Detailed microbubble behaviour at $\sigma = 0.78$ (a) and $\sigma = 0.65$ (b).

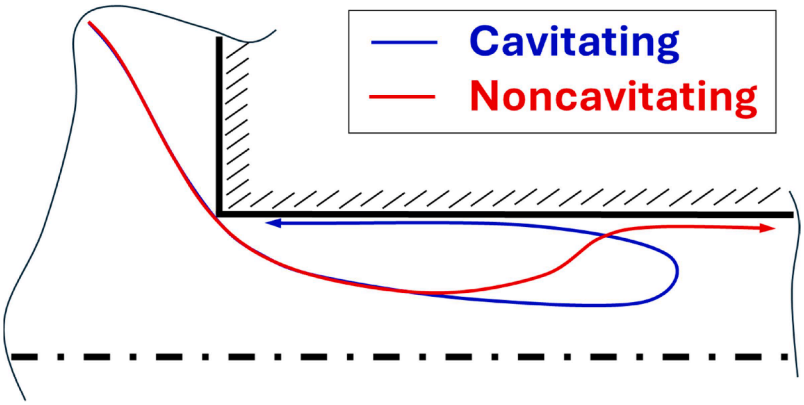

Fig. 22. Modification of the critical streamline under cavitating conditions due to the re-entrant jet.

transport of vapour, which increases the average bubble size in low pressure zones and cannot be considered in the present 1D analysis. What is more, the re-entrant jet effect introduced in the CFD calculation locally increases the vapour concentration in the critical pathline under analysis as depicted in Fig. 22. If the flow pathline obtained from a noncavitating calculation is used, the cavity endpoint is characterized by flow re-attachment (red line). However, when the developed cavitation model is applied, the re-entrant jet is modelled (blue line). This radically changes the pathline shape, convecting downstream vapor back upstream and locally increasing the void fraction (and, consequently, the average bubble radius). In spite of this, the bubble breakup point is faithfully reproduced by the proposed CFD model and shows close

agreement with the analytical solution.

The excellent agreement between the full Rayleigh-Plesset equation and the proposed model, especially at the near-inception conditions of $\sigma = 0.78$, confirms its suitability for the study of microbubble behaviour in the flow which would otherwise be neglected by the Schnerr-Sauer model.

4.5. Influence of turbulence modelling

The presented model is intended to be used in URANS simulations, including compressibility and turbulence corrections such as those provided by equations (5) and (29) for this purpose. However, it can be extended to more resolved approaches such as Detached Eddy Simulation (DES) without altering the modelling assumptions. Keeping the $\sigma = 0.78$ case as the validation benchmark, DES calculations have been performed with both the proposed and the Schnerr-Sauer model.

To maintain consistency with the previously presented URANS results, Delayed Detached Eddy Simulation (DDES) (Spalart et al., 2006) is applied based on the realizable $k-\varepsilon$ model. The compressibility correction for the turbulent viscosity in (5) is kept, and a $C_{DES} = 0.61$ is applied such that:

$$\begin{cases} URANS\ if\ C_{DES}\ max\left(\Delta_x, \Delta_y, \Delta_z\right) > \dfrac{k^{3/2}}{\varepsilon} \\ LES\ if\ C_{DES} max\left(\Delta_x, \Delta_y, \Delta_z\right) \leq \dfrac{k^{3/2}}{\varepsilon} \end{cases} \tag{32}$$

This is, the solver switches between URANS and LES depending on the magnitude of the product of C_{DES} and the maximum cell size, where Δ_i represents the computational cell length in the i^{th} coordinate. In addition, the delayed solution method is used to prevent the activation of LES modelling inside the attached boundary layer, thus avoiding Grid-Induced Separation (GIS) (Menter, 2021). This way, the transport equation for the turbulent kinetic energy in the realizable $k-\varepsilon$ model takes the form:

$$\frac{\partial(\rho_T\, k)}{\partial t} + \nabla\cdot\left(\rho_T\, k\, \vec{V}^{\rightarrow}\right) = \nabla\cdot\left[\left(\mu_T + \frac{\mu_t}{\sigma_k}\right)(\nabla\cdot k)\right] + S_k + E_{DDES} \tag{33}$$

where the turbulent kinetic energy Prandtl number σ_k is set to unity and S_k represents the source term for k. The dissipation term E_{DDES} takes the form:

$$E_{DDES} = -\rho_T\, \varepsilon \max\left(1, \frac{k^{3/2}/\varepsilon}{C_{DES}\Delta}(1 - F_{DDES})\right) \tag{34}$$

with F_{DDES} being 1 for cells inside the boundary layer and 0 elsewhere.

In order to check the validity of the mesh to adequately resolve the turbulent scales, the cell size Δ can be compared to the integral length scale l_0 (Hinze, 1975):

$$l_0 = \frac{k^{3/2}}{\varepsilon} \tag{35}$$

In Fig. 23.a, the ratio between the integral length scale l_0 and the mean mesh size Δ (defined as the cubic root of the computational cell volume) is represented for $\sigma = 0.78$ in the nozzle throat section. It can be checked that the mesh resolution is greater than five cells per length scale. This allows to resolve more than 80% of the turbulent kinetic energy using LES, based on the integration of the Kolmogorov spectrum (Pope, 2013). The mesh resolution is lowest near the cavity interface at the throat section and at the nozzle outlet, with a minimum of $l_0/\Delta = 0.95$ that corresponds to a resolution capability of nearly 40%. As this would mean an insufficient mesh refinement for LES, the calculation method is switched to URANS in these zones as depicted in Fig. 23.b, where the magnitude of the blending function f_b (whose value ranges from zero in pure RANS zones to one in pure LES zones) is represented. Apart from the previously mentioned high-turbulence zones near the cavity interface, it can be checked that the F_{DDES} factor used to protect the boundary layer is being activated near the nozzle wall, where the integral length scale to mesh size ratio would be high enough to allow an adequate LES calculation. However, the blending function f_b is set to zero to prevent grid-induced separation. In the light of the above, the mesh resolution is considered adequate for DES.

Having checked the adequateness of the computational mesh to apply DES, the $\sigma = 0.78$ case can be solved using both the proposed and the Schnerr-Sauer model. The comparison of cavity morphology for both methods is provided in Fig. 24, in which the void fraction contours at the different time steps along a cavity shedding cycle have been represented. When DES is applied, the Schnerr-Sauer formulation (at the bottom of the figure) is able to capture the unsteady shedding dynamics that could not be modelled in the URANS cases of Fig. 13 or Fig. 15. However, the overestimation of cavity length persists together with the neglection of the re-entrant jet. The proposed model, on its part, benefits from a higher resolution level in the Kelvin-Helmholtz instabilities (Podbevšek

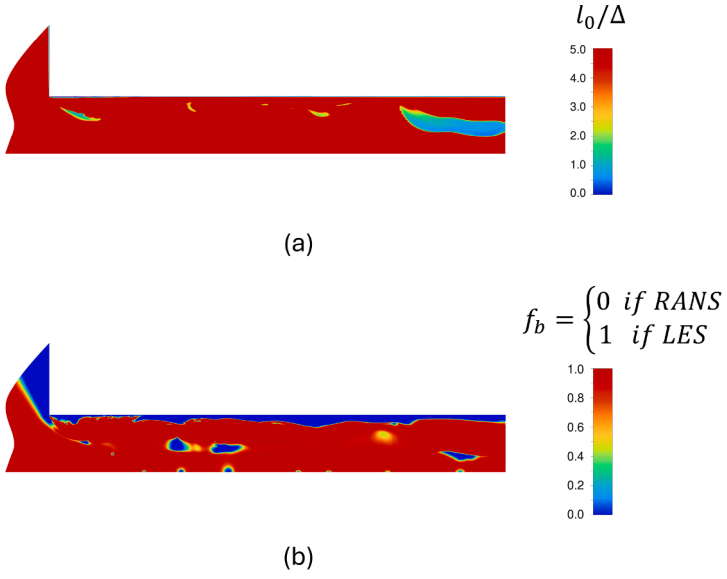

Fig. 23. Integral length scale to mesh size ratio (a) and DES blending function (b) at $\sigma = 0.78$.

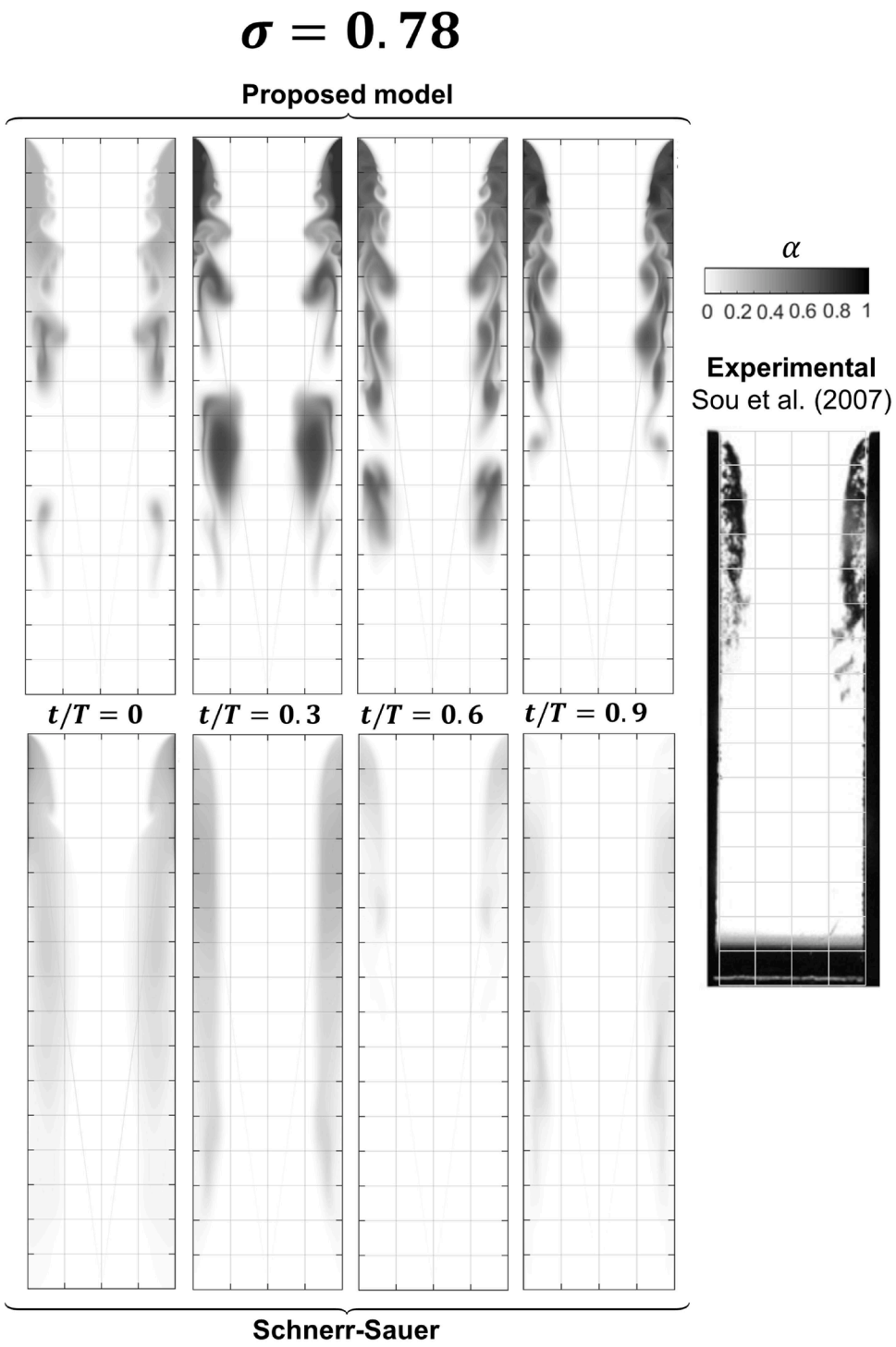

Fig. 24. Cavity evolution at $\sigma = 0.78$ using Delayed Detached Eddy Simulation.

et al., 2021) that develop at the cavity interface, causing cavity shedding downstream the throat section. The re-entrant jet behaviour is still captured, although the liquid jet does not reach the cavity start point as happened in the URANS case of Fig. 13. The cavity length is adequately predicted, as well as the shedding frequency.

Hence, it can be concluded that, even though general improvements are attained for both the Schnerr-Sauer and the proposed formulation using a DES approach, strong differences persist. The presented model significantly improves the capabilities of the Schnerr-Sauer alternative in terms of turbulent interaction, cavity length and re-entrant jet prediction. In addition, it has been checked that it is valid in both URANS and DES approaches, thus being suitable for different applications with variable mesh resolution.

5. Conclusions

A cavitation model based on the Rayleigh-Plesset equation has been derived considering the interaction between bubble size and turbulence by establishing a vapour pressure correction factor. Bubble equilibrium and noncondensable gas effects are also modelled together with the consideration of liquid viscosity. Compressibility corrections of the turbulence model and the influence of slip velocity are also

incorporated. The model has been validated by means of a comparison with the Schnerr-Sauer formulation and the experimental results of Sou et al. achieving close agreement.

The influence of slip velocity and bubble compressibility has proven to be negligible for the studied case. However, the study of bubble slip velocity contours reveals interesting flow features such as the existence of a strong negative slip (opposite to the global flow) zone in the vapour side of the cavity interface while significant positive slip favouring flow acceleration is observed in the liquid side. In this zone, slip velocities more than three times greater than the global flow velocity are observed.

Along the studied range of cavitation numbers, ranging from $\sigma = 1.27$ to $\sigma = 0.55$, the new model consistently improves the results obtained using the Schnerr-Sauer approach, correcting cavitation overestimation at high σ and underestimation at low σ. The re-entrant jet phenomenon is captured in all cases, leading to cavity morphologies in close accordance with the experiments. In addition, the hydraulic flip is modelled at $\sigma = 0.55$, proving that not only the steady cavity behaviour but also the unsteady dynamics are being upgraded.

An improved modelling of individual bubble behaviour (especially at the microscopic scale), the introduction of a dependence of the source term on the initial bubble size that allows to carry out working fluid sensitivity studies and the enhanced cavitation-turbulence interaction can be counted among the strengths of the presented model, all of which are reflected along the validation process. The inclusion of second-order dynamics and bubble nucleation phenomena, as well as bubble-bubble interactions, are neglected and therefore represent an open field for future research and improvement.

CRediT authorship contribution statement

Álvaro Pardo Vigil: Writing – original draft, Visualization, Software, Methodology, Investigation, Conceptualization. **Laura Suárez Fernández:** Visualization, Software, Formal analysis, Data curation. **José González Pérez:** Writing – original draft, Visualization, Supervision, Methodology, Data curation. **Adrián Pandal:** Writing – review & editing, Supervision, Methodology, Formal analysis, Conceptualization.

Declaration of competing interest

The authors declare that they have no known competing financial interests or personal relationships that could have appeared to influence the work reported in this paper.

Acknowledgements

Álvaro Pardo Vigil is supported by the Spanish Ministry of Science, Innovation and Universities within the “FPU” Program (grant reference FPU23/03450). Additional funding is provided by Agencia de Ciencia, Competitividad Empresarial e Innovación Asturiana (Sekuens) within "Subvenciones a Grupos de Investigacion de Organismos Publicos de I+D+I del Principado de Asturias, Convocatoria 2024" (grant reference IDE/2024/000724).

Data availability

The data that support the findings of this study are openly available in Repositorio Institucional de la Universidad de Oviedo at http://doi.org/10.17811/ruo_datasets.79315, reference number 79315.

References

Alamé, K., Mahesh, K., 2024. Effect of gas content on cavitation nuclei. J. Fluid. Mech. 982, A4. https://doi.org/10.1017/jfm.2024.79.
ANSYS, 2024. Relative (Slip) velocity and the drift velocity. Ansys Fluent 2024R1 Theory Guide, pp. 643–645.
Arabnejad, M.H., Nilsson, H., Bensow, R.E., 2023. A novel single-fluid cavitation model with gas content and slip velocity, applied to cavitating tip leakage vortex. Int. J. Multiph. Flow 169. https://doi.org/10.1016/j.ijmultiphaseflow.2023.104619.
Arndt, R.E.A., Keller, A.P., 1976. Free gas content effects on cavitation inception and noise in a free shear flow. In: Proceedings of the IAHR Symposium on Two-Phase Flow and Cavitation in Power Generation.
Bappy, M.H., Carrica, P.M., Vela-Martín, A., Freire, L.S., Buscaglia, G.C., 2020. Pressure statistics of gas nuclei in homogeneous isotropic turbulence with an application to cavitation inception. Phys. Fluids 32. https://doi.org/10.1063/5.0019683.
Biçer, B., Sou, A., 2016. Application of the improved cavitation model to turbulent cavitating flow in fuel injector nozzle. Appl. Math. Model. 40, 4712–4726. https://doi.org/10.1016/j.apm.2015.11.049.
Brandner, P.A., Venning, J.A., Pearce, B.W., 2022. Nucleation effects on cavitation about a sphere. J. Fluid. Mech. 946, A1. https://doi.org/10.1017/jfm.2022.511.
Brennen, C.E., 2013. Cavitation and bubble dynamics. Cambridge University Press. https://doi.org/10.1017/CBO9781107338760.
Brennen, C.E., Christopher, E., 1994. Hydrodynamics of pumps. Concepts ETI.
Callenaere, M., Franc, J.-P., Michel, J.-M., Riondet, M., 2001. The cavitation instability induced by the development of a re-entrant jet. J. Fluid. Mech. 444, 223–256. https://doi.org/10.1017/S0022112001005420.
Chebli, R., Audebert, B., Zhang, G., Coutier-Delgosha, O., 2021. Influence of the turbulence modeling on the simulation of unsteady cavitating flows. Comput. Fluids. 221, 104898. https://doi.org/10.1016/j.compfluid.2021.104898.
Coutier-Delgosha, O., Fortes-Patella, R., Reboud, J.L., 2003. Evaluation of the turbulence model influence on the numerical simulations of unsteady cavitation. J. Fluids Eng. 125, 38–45. https://doi.org/10.1115/1.1524584. Transactions of the ASME.
De Giorgi, M.G., Fontanarosa, D., Ficarella, A., 2019. Characterization of unsteady cavitating flow regimes around a hydrofoil, based on an extended Schnerr-Sauer model coupled with a nucleation model. Int. J. Multiph. Flow 115, 158–180. https://doi.org/10.1016/j.ijmultiphaseflow.2019.03.025.
Fortes-Patella, R., Challier, G., Reboud, J.L., Archer, A., 2013. Energy Balance in Cavitation Erosion: From Bubble Collapse to Indentation of Material Surface. J. Fluids. Eng. https://doi.org/10.1115/1.4023076.
Franc, J.-P., 2007. The Rayleigh-Plesset equation: a simple and powerful tool to understand various aspects of cavitation. In: d’Agostino, L., Salvetti, M.V. (Eds.), Fluid Dynamics of Cavitation and Cavitating Turbopumps. Springer, Vienna.
Gadi Man, Y.A., Trujillo, F.J., 2016. A new pressure formulation for gas-compressibility dampening in bubble dynamics models. Ultrason. Sonochem. 32, 247–257. https://doi.org/10.1016/j.ultsonch.2016.03.013.
Hinze, J.O., McGraw-Hill, Turbulence., 1975. Integral scale turbul. 43–44.
Hsiao, C.-T., Ma, J., Chahine, G.L., 2017. Multiscale tow-phase flow modeling of sheet and cloud cavitation. Int. J. Multiph. Flow 90, 102–117. https://doi.org/10.1016/j.ijmultiphaseflow.2016.12.007.
Issa, R.I., Gosman, A.D., Watkins, A.P., 1986. The computation of compressible and incompressible recirculating flows by a non-iterative implicit scheme. J. Comput. Phys. 62, 66–82. https://doi.org/10.1016/0021-9991(86)90100-2.
Keller, J.B., Miksis, M., 1980. Bubble oscillations of large amplitude. J. Acoust. Soc. Am. 68, 628–633. https://doi.org/10.1121/1.384720.
Koukouvinis, P., Gavaises, M., Supponen, O., Farhat, M., 2016. Numerical simulation of a collapsing bubble subject to gravity. Phys. Fluids 28. https://doi.org/10.1063/1.4944561.
Langley, D.S., 1984. Light Scattering from Bubbles in Liquids. Washington State University.
Levi, D.M., 2011. Visual Acuity. In: Lewin, L.E., Nilsson, S.F.E., Ver Hoeve, J., Wu, S.M. (Eds.), Adler’s Physiology of the Eye. Elsevier Mosby, pp. 627–647.
Li, Wei, Yang, Y., Shi, W.D., Zhao, X., Li, Weiqiang, 2018. The correction and evaluation of cavitation model considering the thermodynamic effect. Math. Probl. Eng. 2018. https://doi.org/10.1155/2018/7217513.
Liu, Z., Brennen, C.E., 1998. Cavitation nuclei population and event rates. J. Fluids Eng., Trans. ASME 120, 728–737. https://doi.org/10.1115/1.2820730.
Lyu, X., 2020. Numerical Modeling and Simulation of Cavitation Bubble Cloud with a Lagrangian-Eulerian Approach.
Manickam, S., Ashokkumar, M., 2014. Cavitation : a novel energy-efficient technique for the generation of nanomaterials.
Maninnen, M., Taivassalo, V., Kallio, S., 1996. On the Mixture Model for Multiphase Flow. VTT Julkaisija Utgivare Publisher.
Menter, F.R., 2021. Best practice: scale-resolving simulations in ansys CFD.
Menter, F.R., Sechner, R., 2021. Two-equation models: limiters. Best Practice: RANS Turbulence Modeling in Ansys CFD, pp. 85–86.
Morsi, S.A., Alexander, A.J., 1972. An investigation of particle trajectories in two-phase flow systems. J. Fluid. Mech. 55, 193. https://doi.org/10.1017/S0022112072001806.
Mousmoulis, G., Karlsen-Davies, N., Aggidis, G., Anagnostopoulos, I., Papantonis, D., 2019. Experimental analysis of cavitation in a centrifugal pump using acoustic emission, vibration measurements and flow visualization. Eur. J. Mech. - B/Fluids 75, 300–311. https://doi.org/10.1016/J.EUROMECHFLU.2018.10.015.
Muzaferija, S., Papoulias, D., Peric, M., 2017. VOF simulations of hydrodynamic cavitation using the asymptotic and classical rayleigh-plesset models.
O’Hern, T.J., 1987. Cavitation inception scale effects.
Pearsall, I.S., 1972. Cavitation. Mills and Boon.
Plesset, M.S., 1949. The Dynamics of Cavitation Bubbles. J. Appl. Mech. 16, 277–282. https://doi.org/10.1115/1.4009975.
Podbevšek, D., Petkovšek, M., Ohl, C.D., Dular, M., 2021. Kelvin-Helmholtz instability governs the cavitation cloud shedding in Venturi microchannel. Int. J. Multiph. Flow 142, 103700. https://doi.org/10.1016/j.ijmultiphaseflow.2021.103700.

Pope, S.B., 2013. The scales of turbulent motion. Turbulent Flows. Cambridge University Press, Cambridge, pp. 182–263.
Rayleigh, Lord, 1917. On the pressure developed in a liquid during the collapse of a spherical cavity. Lond. Edinb. Dublin Philos. Mag. J. Sci. 34, 94–98. https://doi.org/10.1080/14786440808635681.
Roache, P.J., 1994. Perspective: a method for uniform reporting of grid refinement studies. J. Fluids. Eng. 116, 405–413. https://doi.org/10.1115/1.2910291.
Sauer, J., 2000. Ein neues Modell, basierend auf Front Capturing (VoF) und Blasendynamik. Fakultät für Maschinenbau der Universität Karlsruhe, Karlsruhe.
Savio, A., Cianferra, M., Armenio, V., 2021. Analysis of performance of cavitation models with analytically calculated coefficients. Energies (Basel) 14, 6425. https://doi.org/10.3390/en14196425.
Schnerr, G.H., Sauer, J., 2001. Physical and numerical modeling of unsteady cavitation dynamics. In: 4th International Conference on Multiphase Flow. New Orleans.
Singhal, A.K., Athavale, M.M., Li, H., Jiang, Y., 2002. Mathematical basis and validation of the full cavitation model. J. Fluids. Eng. 124, 617–624. https://doi.org/10.1115/1.1486223.
Sou, A., Biçer, B., Tomiyama, A., 2014. Numerical simulation of incipient cavitation flow in a nozzle of fuel injector. Comput. Fluids. 103, 42–48. https://doi.org/10.1016/j.compfluid.2014.07.011.
Sou, A., Hosokawa, S., Tomiyama, A., 2007. Effects of cavitation in a nozzle on liquid jet atomization. Int. J. Heat. Mass Transf. 50, 3575–3582. https://doi.org/10.1016/j.ijheatmasstransfer.2006.12.033.
Spalart, P.R., Deck, S., Shur, M.L., Squires, K.D., Strelets, M.Kh., Travin, A., 2006. A new version of detached-eddy simulation, resistant to ambiguous grid densities. Theor. Comput. Fluid. Dyn. 20, 181–195. https://doi.org/10.1007/s00162-006-0015-0.
Susan-Resiga, R., Ciocan, G.D., Avellan, F., 2004. Swirling flow downstream a Francis turbine runner. In: The 6th International Conference on Hydraulic Machinery and Hydrodynamics. Polytechnic University of Timisoara, Timisoara.
Trummler, T., Schmidt, S.J., Adams, N.A., 2020. Investigation of condensation shocks and re-entrant jet dynamics in a cavitating nozzle flow by Large-Eddy Simulation. Int. J. Multiph. Flow 125, 103215. https://doi.org/10.1016/j.ijmultiphaseflow.2020.103215.
Uberoi, M.S., 1953. Quadruple velocity correlations and pressure fluctuations in isotropic turbulence. J. Aeronaut. Sci. 20, 197–204. https://doi.org/10.2514/8.2589.
Vallier, A., 2013. Simulations of Cavitation - From the Large Vapour Structures to the Small Bubble Dynamics. Division of Fluid Mechanics, Department of Energy Sciences, Faculty of Engineering, Lund University.
Venning, J.A., Pearce, B.W., Brandner, P.A., 2022. Nucleation effects on cloud cavitation about a hydrofoil. J. Fluid. Mech. 947, A1. https://doi.org/10.1017/jfm.2022.535.
Viitanen, V., Sipilä, T., Sánchez-Caja, A., Siikonen, T., 2022. CFD predictions of unsteady cavitation for a marine propeller in oblique inflow. Ocean Eng. 266. https://doi.org/10.1016/j.oceaneng.2022.112596.
Wang, Z., Cheng, H., Ji, B., 2021. Euler-Lagrange study of cavitating turbulent flow around a hydrofoil. Phys. Fluids 33. https://doi.org/10.1063/5.0070312.
Wang, Z., Cheng, H., Ji, B., Peng, X., 2023. Numerical investigation of inner structure and its formation mechanism of cloud cavitating flow. Int. J. Multiph. Flow 165, 104484. https://doi.org/10.1016/j.ijmultiphaseflow.2023.104484.
Wu, Y., Zhu, D., Tao, R., Xiao, R., Liu, W., 2022. Analysis of two-phase flow in cavitation condition of pump-turbine based on dynamic mode decomposition method in turbine mode. J. Energy Storage 56, 106107. https://doi.org/10.1016/j.est.2022.106107.
Yamashita, T., Ando, K., 2019. Low-intensity ultrasound induced cavitation and streaming in oxygen-supersaturated water: role of cavitation bubbles as physical cleaning agents. Ultrason. Sonochem. 52, 268–279. https://doi.org/10.1016/j.ultsonch.2018.11.025.
Yunqiao, L., Hao, Z., Wei, Z., Benlong, W., 2023. Bubble size distribution at early stage of hydrodynamic cloud cavitation. Phys. Fluids 35. https://doi.org/10.1063/5.0154309.
Zhao, X., Cheng, H., Ji, B., Li, L., Bensow, R.E., 2024. Insights into the characteristics of sheet/cloud cavitation and tip-leakage cavitation based on a compressible Euler-Lagrange model. Phys. Rev. Fluids. 9, 104304. https://doi.org/10.1103/PhysRevFluids.9.104304.
Zwart, P.J., Gerber, A.G., Belamri, T., 2004. A two-phase flow model for predicting cavitation dynamics. In: ICMF 2004 International Conference on Multiphase Flow. Yokohama.